



HAL
open science

Modified chromosome structure caused by phosphomimetic H2A modulates the DNA damage response by increasing chromatin mobility in yeast

Fabiola García Fernández, Brenda Lemos, Yasmine Khalil, Renaud Batrin, James Haber, Emmanuelle Fabre

► To cite this version:

Fabiola García Fernández, Brenda Lemos, Yasmine Khalil, Renaud Batrin, James Haber, et al.. Modified chromosome structure caused by phosphomimetic H2A modulates the DNA damage response by increasing chromatin mobility in yeast. *Journal of Cell Science*, 2021, 134 (6), 10.1242/jcs.258500 . hal-03455314

HAL Id: hal-03455314

<https://hal.science/hal-03455314v1>

Submitted on 30 Nov 2021

HAL is a multi-disciplinary open access archive for the deposit and dissemination of scientific research documents, whether they are published or not. The documents may come from teaching and research institutions in France or abroad, or from public or private research centers.

L'archive ouverte pluridisciplinaire **HAL**, est destinée au dépôt et à la diffusion de documents scientifiques de niveau recherche, publiés ou non, émanant des établissements d'enseignement et de recherche français ou étrangers, des laboratoires publics ou privés.

RESEARCH ARTICLE

Modified chromosome structure caused by phosphomimetic H2A modulates the DNA damage response by increasing chromatin mobility in yeast

Fabiola García Fernández¹, Brenda Lemos², Yasmine Khalil¹, Renaud Batrin¹, James E. Haber² and Emmanuelle Fabre^{1,*}

ABSTRACT

In budding yeast and mammals, double-strand breaks (DSBs) trigger global chromatin mobility together with rapid phosphorylation of histone H2A over an extensive region of the chromatin. To assess the role of H2A phosphorylation in this response to DNA damage, we have constructed strains where H2A has been mutated to the phosphomimetic H2A-S129E. We show that mimicking H2A phosphorylation leads to an increase in global chromatin mobility in the absence of DNA damage. The intrinsic chromatin mobility of H2A-S129E is not due to downstream checkpoint activation, histone degradation or kinetochore anchoring. Rather, the increased intrachromosomal distances observed in the H2A-S129E mutant are consistent with chromatin structural changes. Strikingly, in this context the Rad9-dependent checkpoint becomes dispensable. Moreover, increased chromatin dynamics in the H2A-S129E mutant correlates with improved DSB repair by non-homologous end joining and a sharp decrease in interchromosomal translocation rate. We propose that changes in chromosomal conformation due to H2A phosphorylation are sufficient to modulate the DNA damage response and maintain genome integrity.

This article has an associated First Person interview with the first author of the paper.

KEY WORDS: Chromatin dynamics, Double-strand break repair, Epigenetics

INTRODUCTION

Eukaryotic cells have developed sophisticated machineries to respond to the multiple stresses they are constantly confronted with. In the presence of DNA double-strand breaks (DSBs), the DNA damage response (DDR) protects the genome by detecting and repairing the potentially lethal DSBs that could lead to genome instability or tumorigenesis. Inherited or acquired defects in the DDR can result in various diseases, such as immune deficiency, neurological degeneration, premature aging and severe cancer susceptibility (reviewed in Goldstein and Kastan, 2015; Jackson and Bartek, 2009).


The DDR starts with the recruitment of surveillance proteins that activate cell cycle checkpoints, promote chromatin remodeling allowing DNA accessibility to the repair machinery and trigger DNA repair pathway choice (Aylon and Kupiec, 2004; Ceccaldi et al., 2016; Mehta and Haber, 2014; Symington and Gautier, 2011). Two of the most well-known DSB repair mechanisms are homologous recombination (HR) and non-homologous end joining (NHEJ). Whereas HR repairs DNA breaks by copying the missing information across the lesion from an undamaged template, as from the replicated sister chromatid, NHEJ repairs breaks by ligation of the broken ends after their juxtaposition (Aylon and Kupiec, 2004; Ceccaldi et al., 2016; Mehta and Haber, 2014; Symington and Gautier, 2011). Long considered as error-prone, the classical form of NHEJ is now regarded as a versatile, adaptable and essential pathway for the maintenance of genomic stability, because joining of the juxtaposed ends of the breaks does not necessarily involve nucleotide deletions. However, alternative forms of end joining exist that can induce DNA aberrations, including chromosomal translocations (reviewed in Bétermier et al., 2014; Emerson and Bertuch, 2016; Mcvey et al., 2008).

To repair the damage, the DNA damage checkpoint delays cell cycle progression. This delay can trigger arrests at the G1-S transition, during the S phase or at the G2-M transition, depending on the nature of the damage and the phase of the cell cycle in which the lesion happens (for reviews see Finn et al., 2012; Shaltiel et al., 2015; Waterman et al., 2019). The highly conserved MRX^{MRN} complex (MRX in yeast, comprising Mre11–Rad50–Xrs2; MRN in mammals, comprising MRE11–RAD50–NBS1) is among the earliest sensors of DSB and binds directly to broken ends of DNA. Sensing includes activation of the phosphatidylinositol 3-kinase-related kinase (PIKK) family, such as mammalian ATM (ataxia-telangiectasia mutated) and ATR (ATM- and Rad3-related), or their budding yeast orthologs Tel1 and Mec1. These sensing kinases are required independently after a DSB, at different points of the DDR. Tel1^{ATM} is rapidly recruited and activated after the recognition of the DSB by the MRX^{MRN} complex, whereas Mec1^{ATR} is recruited by the ATR-interacting protein Ddc2 (also known as Lcd1; ortholog of mammalian ATRIP) after 5' to 3' resection of the DSB ends yields single-stranded DNA and binding of RPA (Kondo et al., 2001; Li et al., 2020; Nakada et al., 2003; Shroff et al., 2004; Tibbetts et al., 1999; Zhou and Elledge, 2000). Both kinases phosphorylate several other proteins involved in cell cycle checkpoint control and DNA repair. An important landmark is the phosphorylation of histone H2A in yeast and of histone variant H2AX in mammals [here referred to collectively as H2A(X)]. Phosphorylation of histone H2A(X) occurs near its C terminus (S129 in yeast H2A and S139 in mammalian H2AX; Burma et al., 2001; Celeste et al., 2003; Redon et al., 2003; Rossetto et al., 2012;

¹Institut de recherche Saint-Louis (IRSL), Université de Paris, INSERM U944, CNRS UMR7212, Genome and Cell Biology of Diseases Unit, F-75010 Paris, France.

²Department of Biology and Rosenstiel Basic Medical Sciences Research Center, Brandeis University, Waltham, MA 02454-9110, USA.

*Author for correspondence (emmanuelle-g.fabre@inserm.fr)

 Y.K., 0000-0002-7640-1703; E.F., 0000-0002-0009-4604

Handling Editor: Maria Carmo-Fonseca
Received 5 February 2021; Accepted 6 February 2021

Shroff et al., 2004). Phosphorylated H2A(X) in yeast and mammals, also known as γ -H2A(X), rapidly accumulates at the DSB, spreads over long distances and contributes to further DNA signaling and repair (Burma et al., 2001; Downs et al., 2000; Lee et al., 2014; Renkawitz et al., 2013; Shroff et al., 2004).

Phosphorylation of H2A(X) at the site of a DSB allows recruitment of chromatin remodeling complexes (such as the INO80 and SWR1 complexes) and downstream checkpoint proteins, including 53BP1 (also known as TP53BP1; the ortholog of yeast Rad9) (Hammett et al., 2007; Morrison et al., 2004; Tsukuda, 2005; Van Attikum et al., 2004). Rad9^{53BP1} is a critical checkpoint adaptor protein that transmits the signal from Mec1^{ATR} and Tel1^{ATM} to the downstream effectors Rad53^{CHK2} and Chk1^{CHK1} (Blankley and Lydall, 2004; Harrison and Haber, 2006; Sweeney et al., 2005). Rad9 was originally identified in a pioneering study in budding yeast, where it controls cell cycle progression by arresting cells in the G2/M phase in case of unrepaired damage (Weinert and Hartwell, 1988). Rad9 and 53BP1 both contain BRCT and Tudor domains that recognize histone H3 methylation and γ -H2A(X) phosphorylation, respectively (Hammett et al., 2007; Lancelot et al., 2007). The protective role of Rad9 in genome integrity is evidenced by the poor survival of $\Delta rad9$ mutants upon genotoxic treatments including phleomycin, γ -rays and UV (Menin et al., 2019; Mirman and de Lange, 2020). Moreover, Rad9^{53BP1} deletion results in a faster degradation of DSB ends, which disfavors NHEJ repair (Ferrari et al., 2015; Lazzaro et al., 2008; Zimmermann and De Lange, 2014).

DDR activation leads to dynamic modifications in chromatin structure, which have been implicated in the activation and transduction of the checkpoint cascade; however, neither the functional relevance of chromatin modifications nor the mechanisms by which the DDR is activated by chromatin itself is fully understood. It has been shown that robust targeting of repair factors or kinase sensors, in the absence of damage, can elicit the DDR both in yeast or in mammals, indicating that local concentration of sensor protein and/or the higher order of chromatin structure are key in the DDR cascade (Bonilla et al., 2008; Soutoglou and Misteli, 2008). In fact, in mammals, chromatin at the site of damage experiences two successive waves of changes. A first local expansion dependent on γ -H2AX and the MRN complex is followed by a dynamic compaction, the latter being enough to activate the DDR (Burgess et al., 2014; Khurana et al., 2014; Kruhlak et al., 2006; Ziv et al., 2006). Chromatin compaction, due to the tethering of methyltransferase SUV3-9 (also known as SUV39H1) or heterochromatin protein HP1 β (also known as CBX1), can trigger ATM signaling and activate upstream (γ -H2AX) but not downstream (53BP1) components of the DDR cascade, showing that chromatin compaction is an integral step of the DDR (Burgess et al., 2014). Strikingly, a global alteration of chromatin and chromosome structure, induced by hypotonic condition or mechanical stress, is sufficient to activate ATM or ATR in the absence of any DNA damage, respectively (Bakkenist and Kastan, 2003; Kumar et al., 2014). Yeast lacks homologs of SUV3-9 or HP1 β , but interestingly, Mec1 might respond to chromatin dynamics during S phase, when replication stress occurs and causes mechanical stress on the nuclear membrane (Bermejo et al., 2011; Forey et al., 2020).

Global modification of damaged genomes is also evidenced through an increase of chromosome mobility, a process that may favor repair in yeast (Hauer et al., 2017; Herbert et al., 2017; Lawrimore et al., 2017; Miné-Hattab and Rothstein, 2012; Seeber et al., 2013; Smith et al., 2018; Strecker et al., 2016). The molecular mechanisms that play a role in global mobility are not fully deciphered, but regulatory networks are becoming clearer (reviewed

in Haber, 2018; Seeber et al., 2018; Smith and Rothstein, 2017; Zimmer and Fabre, 2019). The DDR activation by Mec1^{ATR} and Tel1^{ATM} is a critical first step in the response (Dion et al., 2012; Miné-Hattab and Rothstein, 2012; Seeber et al., 2013; Smith et al., 2018). Mec1^{ATR} and Tel1^{ATM} activation have diverse consequences, such as centromeric relaxation (Lawrimore et al., 2017; Strecker et al., 2016) and chromatin modifications (Hauer et al., 2017; Herbert et al., 2017; Miné-Hattab et al., 2017). It has been proposed that the repulsive forces of the negative charges resulting from H2A phosphorylation or the Rad51 repair protein could regulate chromatin stiffening both locally and globally (Herbert et al., 2017; Miné-Hattab et al., 2017), and that histone depletion could be the cause of a more expanded chromatin (Cheblal et al., 2020; Hauer et al., 2017), both chromatin alterations resulting in the observed increase of chromosome mobility. It is remarkable that increased chromosome mobility as a response to genomic insults is a conserved feature in metazoan genomes, with regulation involving the repair protein 53BP1 or γ -H2AX, similar to the response in yeast (Clouaire et al., 2018; Dimitrova et al., 2008; Lotterberger et al., 2015; Ryu et al., 2015; Schrank et al., 2018).

To better understand how γ -H2A(X) affects different aspects of chromosome structure and movement, we have created yeast strains in which both copies of the H2A-encoding genes have been mutated to S129E, which appears to be phosphomimetic (Eapen et al., 2012). We find that H2A-S129E fully recapitulates the increased apparent stiffness of chromatin observed after damage, resulting in increased intrachromosomal distances and chromosome dynamics. An increased repair by NHEJ and a decreased rate of translocation correlate with this change in chromatin. Surprisingly, we find that H2A-S129E rescues $\Delta rad9$ survival deficiency and cell cycle checkpoint defects after DNA damage, further supporting the notion that changes in chromatin structure are a key contributor to the DDR.

RESULTS

In the absence of DNA damage, mimicking H2A phosphorylation increases chromosome mobility

To study the consequences of mimicking H2A-S129 phosphorylation on chromosome mobility, we created isogenic yeast strains in which both *HTA1* and *HTA2* were mutated to encode H2A-S129E using CRISPR/Cas9-mediated gene editing (see Materials and Methods). We used four strains (P1–P4) that carry fluorescently labeled green loci (LacI–GFP bound to an array of *lacO* sites) at different regions of the right arm of chromosome IV (Fig. 1A). As control, we replaced S129 with an alanine to impede phosphorylation, using the same strategy (H2A-S129A). We first compared the growth of the H2A-S129 mutants to their wild-type (WT) counterpart, in the presence or in the absence of DNA damage generated by the radiomimetic drug Zeocin (Dion et al., 2012; Herbert et al., 2017; Seeber et al., 2013). In the absence of Zeocin, growth rates of P1–P4 WT, H2A-S129E and H2A-S129A strains were indistinguishable, suggesting no particular endogenous damage caused by these mutations. WT strains exhibited a sensitivity to Zeocin (Fig. 1A; Fig. S1A). In the presence of Zeocin, growth of H2A-S129E was similar to that of WT, whereas H2A-S129A mutants showed increased sensitivity (Fig. 1A; Fig. S1A). To precisely measure the sensitivity to Zeocin of the mutant strains, we performed colony forming unit (CFU) assays by calculating the ratio between colonies grown on media with and without Zeocin. CFU ratios were close to 70% in P1–P4 WT cells (Fig. 1B). Likewise, CFU ratios in H2A-S129E mutant strains ranged between 81% \pm 3.1 and 96% \pm 3.2 (mean \pm s.d.), with no

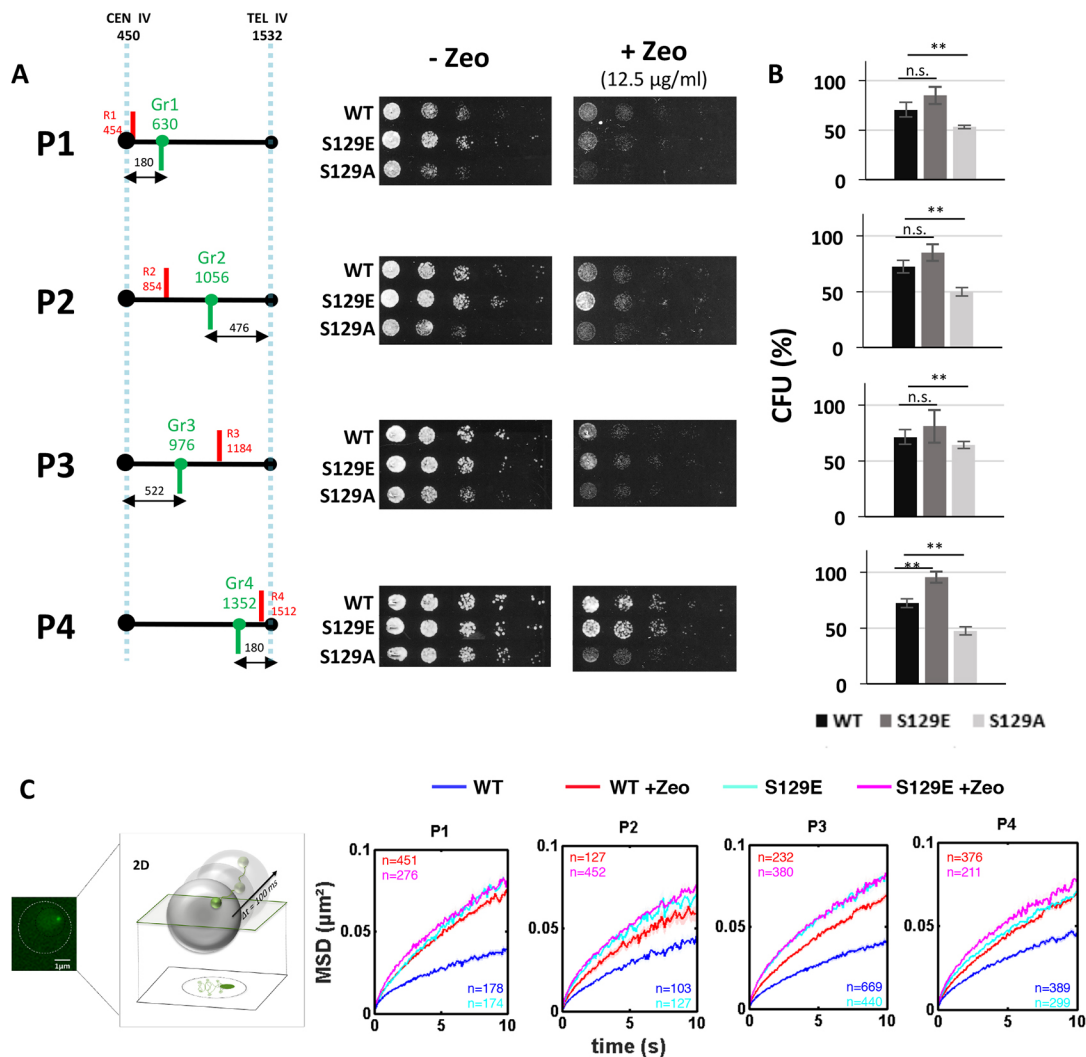


Fig. 1. H2A-S129E increases global chromatin dynamics in absence of DNA damage. (A) Left: schematics of chromosome IV, indicating the genomic positions of fluorescently labeled loci investigated in this study. Features are labeled with their genomic position in kb. Blue dashed lines indicate the centromere (CEN IV) and the right telomere (TEL IV). Red and green bars indicate the four loci tagged in red (R1–R4) or green (Gr1–Gr4). Numbers above the arrows indicate the genomic distance of each green-tagged locus from the centromere or telomere in kb. Strains P1 to P4 correspond to individual red–green pairs, separated by ~200 kb (R1–Gr1, R2–Gr2, Gr3–R3 and Gr4–R4, respectively). Right: drop assays (left to right, tenfold dilutions) showing comparable growth of WT and H2A-S129E mutants in the absence of damage (–Zeo) and comparable sensitivity to long exposure to Zeocin (12.5 µg/ml; +Zeo). As a control, effect of the Zeocin on cell survival is shown for H2A-S129A mutants. (B) Colony forming units (CFU), calculated as the percentage of grown colonies in the presence of Zeocin relative to grown colonies in the absence of Zeocin, after spreading of ~200 colonies for each condition for the four strains tested (P1–P4) in wild-type (WT, black bars), H2A-S129E mutants (gray bars) and H2A-S129A mutants (light gray bars). Data are presented as mean±s.d. of at least three independent experiments. ** $P \leq 0.01$; n.s., not significant (non-parametric *t*-test). (C) Left: example image (dashed line indicates cell outline) and schematic showing the 2D time-lapse imaging protocol. Right: mean square displacements (MSDs) of WT cells and H2A-S129E mutants (S129E) as function of time interval for the four green loci in P1 to P4 strains, as computed from 2D time-lapse microscopy data (cell population mean±s.e.m.). Blue and red curves are for untreated and Zeocin-treated WT cells, respectively; cyan and magenta curves are for untreated and Zeocin-treated H2A-S129E mutant cells, respectively. The numbers of cells used to calculate each curve (*n*) are indicated.

significant difference from WT, except for the P4 strain, which showed a slightly higher survival (Downs et al., 2000; Moore et al., 2007; Redon et al., 2003). In H2A-S129A strains, CFU ranged from 47.5%±4.0 to 64.5%±7.2 confirming the enhanced sensitivity of these mutants to Zeocin compared to that of WT cells. The simplest interpretation for a similar survival after DNA damage of H2A-S129E mutants and WT is that glutamic acid can replace the function normally provided by S129 phosphorylation, a conclusion further supported by analysis of the H2A-S129A mutants.

We then explored chromosome mobility in H2A-S129E mutant cells by tracking the fluorescently labeled green loci (Herbert et al., 2017). Green labels were located at 180 kb and 522 kb from

centromere IV, or at 476 kb and 180 kb from the right telomere IV (Gr1, Gr3, Gr2 and Gr4, respectively; Fig. 1A). We analyzed mean square displacements (MSDs) of the four Gr1–Gr4 loci by tracking hundreds of cells in each P1–P4 strain, using high-speed 100 ms time-lapse microscopy, for a time period of 5 min (Herbert et al., 2017; Spichal et al., 2016). To induce DNA damage, we used a final concentration of Zeocin of 250 µg/ml for 6 h. Under these conditions, in which ~80% of the cell population showed damage, as seen by Rad52–GFP foci formation (Fig. S1B; Herbert et al., 2017), WT cells exhibited a global increase in chromosome mobility (Fig. 1C). Strikingly, in the absence of Zeocin treatment, the MSDs in the H2A-S129E mutant strains were

as high as those observed in WT strains after induction of damage (Fig. 1C; Fig. S2A). In these mutant cells, addition of Zeocin for 6 h did not significantly increase MSDs, suggesting that H2A-S129E mutation maximizes mobility that Zeocin cannot increase any further (Fig. 1C; Fig. S2A). After Zeocin exposure, the lower increase in mobility of the four tagged Gr1–Gr4 loci in H2A-S129A mutant cells (Fig. S2B,C) confirmed that γ -H2A is required for full global mobility upon DNA damage (Herbert et al., 2017). Taken together, these results suggest that the function normally performed by H2A phosphorylation is mirrored by H2A-S129E and that this mutation is sufficient to induce an increase in chromosomal dynamics.

The H2A-S129E mutation does not trigger cell cycle arrest, histone loss or centromere detachment

To understand the mechanism underlying the enhanced dynamics observed in the H2A-S129E mutant, we explored different hypotheses. First, it is well documented that checkpoint activation induces global mobility upon DNA damage (Hauer et al., 2017; Seeber et al., 2013; Smith et al., 2018). To test whether the H2A-S129E mutant inherently activates a cell cycle checkpoint, we explored the effect of this mutant on cell cycle progression. Results of FACS assays using asynchronous populations indicated an equally low number (19–23%) of cells in the G2/M cell cycle phase in the WT and H2A-S129E mutant strains, indicating that the DDR checkpoint leading to cell cycle arrest is not activated in the H2A-S129E mutant (Fig. 2A). In addition, phosphorylation of Rad53, the signal for effective checkpoint activation (Pelliccioli et al., 2001), was not observed in both strains in the absence of damage (Fig. 2A). However, both WT and H2A-S129E mutant strains exhibited a similar DNA damage response after 6 h Zeocin treatment, since the percentage of G2/M-arrested cells was enriched (71–77%) in both strains, with an accompanying hyper-phosphorylation of Rad53 (Fig. 2A; Fig. S3A). These results reject the hypothesis that enhanced chromatin dynamics observed in H2A-S129E mutants in the absence of damage is triggered by constitutive activation of the cell cycle checkpoint. Second, histone loss has been shown to elicit enhanced chromatin mobility (Hauer et al., 2017). We therefore examined the global stability of histones. By immunoblotting, we found comparable levels of total histone H4 in WT and H2A-S129E mutant cells (Fig. 2B). Total histone H4 abundance strongly decreased upon 6 h of Zeocin treatment, as previously reported (Fig. 2B; Hauer et al., 2017). These results ascertained that enhanced mobility observed in H2A-S129E mutants cannot be explained by histone instability and, together with the FACS analyses, showed that WT and the H2A-S129E mutant respond to damage in a similar manner. Finally, a previous study has shown that induction of a single DSB in the genome leads to kinetochore protein Cep3 phosphorylation by Mec1 and also correlates with an increase in global mobility associated with an increase in spindle pole body (SPB)–centromere 2D distances (Strecker et al., 2016). We therefore measured the distances between Spc42, a protein of the SPB, fused to mCherry and CenIV labeled by an array of *tetO* repeats bound by TetR–GFP (He et al., 2000). In the absence of Zeocin, the SPB–CenIV distances for WT and H2A-S129E strains were identical, and in both cases the distances increased after cells were treated with Zeocin (Fig. 2C), indicating that a general loosening of the anchoring of the centromeres to the SPB is probably not the cause of the increase in chromosomal mobility observed in H2A-S129E mutants. Thus, the high intrinsic mobility of H2A-S129E mutated chromatin must be due to factors other than checkpoint activation, histone degradation or loosening of centromere tethering to the SPB.

Mimicking H2A-S129 phosphorylation increases intrachromosomal distances without DNA damage

It has been established that increases in genomic mobility can be explained by changes in chromatin structure (Hauer et al., 2017; Herbert et al., 2017; Miné-Hattab et al., 2017). Based on polymer modeling and multi-scale tracking of chromatin after damage, a global stiffening of the chromatin fiber is consistent with a simultaneous increase in chromosomal mobility and spatial distances between loci on the same chromosome (Herbert et al., 2017; Miné-Hattab et al., 2017). H2A phosphorylation has been proposed as a potential molecular mechanism, since the negative repulsive charges due to H2A phosphorylation could increase the stiffness of the chromatin fiber, as seen *in vitro* and by modeling (Cui and Bustamante, 2000; Herbert et al., 2017; Qian et al., 2013). In addition, based on similar experiments, but using different modeling assumptions, chromatin decompaction has also been proposed to play a role (Amitai et al., 2017; Hauer et al., 2017). We therefore hypothesized that the increase in H2A-S129E chromosome motion could be linked to a change in chromosomal structure. To address this question, we measured red–green pairwise distances in P1–P4 WT and H2A-S129E mutated strains (Fig. 2D). In these strains, *tetO* arrays bound by TetR–mRFP were inserted ~200 kb from the green labels (see Fig. 1A). As expected, intrachromosomal distances increased in WT strains after prolonged treatment with Zeocin (3 h), ranging from ~350–414 nm to ~384–628 nm in the absence and presence of Zeocin, respectively (Fig. 2D; Herbert et al., 2017). In the absence of Zeocin treatment, increased intrachromosomal distances (~396–496 nm) were observed all along the chromosome arm in H2A-S129E mutants, similar to those observed in WT upon Zeocin treatment (Fig. 2D). In contrast, intrachromosomal distances do not increase in H2A-S129A mutants (Herbert et al., 2017), showing that the effect on distances is specific to H2A-S129E mutation. A structural change in chromatin is accordingly the most probable cause for the increased mobility observed in the H2A-S129E mutant, in the absence of any DNA damage.

Rad9 checkpoint control of cell survival and global mobility upon Zeocin treatment is suppressed by mimicking H2A phosphorylation

The observation that H2A-S129E causes an increase in chromosome dynamics independent of cell cycle arrest suggests that structural changes in the chromatin of this mutant may make checkpoint factors dispensable for damage-induced chromatin mobility (Bonilla et al., 2008; Dion et al., 2012; Miné-Hattab and Rothstein, 2012; Seeber et al., 2013; Smith et al., 2018). To test this hypothesis, we mutated the key checkpoint adaptor Rad9, which mediates the interaction between modified histones, such as γ -H2A, and several effector proteins in the DDR (Finn et al., 2012). We deleted *RAD9* in the WT and H2A-S129E P2 strains and analyzed single ($\Delta rad9$) and double ($\Delta rad9$ H2A-S129E) mutant cell survival, cell cycle profile and chromosome mobility phenotypes. In the absence of Zeocin treatment, both mutants grew similarly to their wild-type *RAD9* counterpart in spot assays (Fig. 3A). As expected, the growth of the $\Delta rad9$ mutant was affected in the presence of Zeocin. Interestingly, spot assays and CFU ratio quantification of treated versus non-treated cells indicated that the $\Delta rad9$ H2A-S129E double mutant was indistinguishable from WT or the H2A-S129E single mutant strain (Fig. 3A,B). Moreover, while cell cycle arrest due to Zeocin was deficient in the $\Delta rad9$ mutant, as predicted, it was restored in the $\Delta rad9$ H2A-S129E double mutant (after Zeocin treatment, $P=0.49$ between WT and

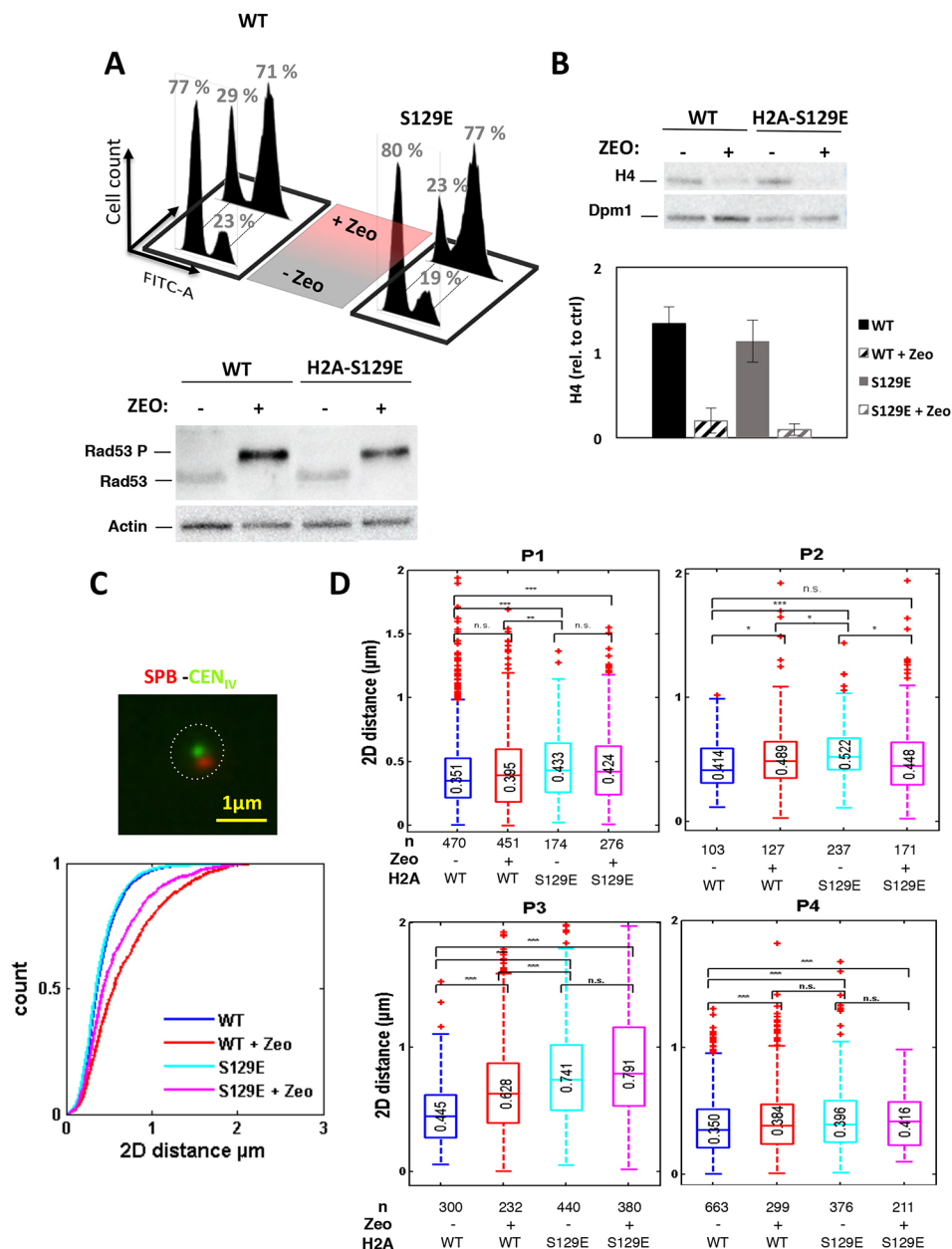


Fig. 2. The increase in global chromatin dynamics in H2A-S129E mutant cells is not linked to checkpoint activation, histone loss or defective centromeric tethering but to increased intrachromosomal distances. (A) Top: flow cytometry analysis of asynchronous WT and H2A-S129E mutant cell populations either untreated (-Zeo) or treated with Zeocin (+Zeo). H2A-S129E mutants show normal cell cycle (most cells low FITC-A) in the absence of damage and G2/M arrest (most cells high FITC-A) in the presence of damage, similar to the WT. The percentage of cells in the low and high FITC-A populations are indicated, based on three experiments. Statistical analyses of differences between WT and H2A-S129E-mutated cells using a chi-square test showed non-significant values of 0.32 and 0.15 for untreated and treated conditions, respectively. Bottom: representative results from immunoblotting showing the phosphorylation status (P) of Rad53-HA in WT and H2A-S129E cells in response to Zeocin treatment. Actin was used as a loading control. Blots are representative of three experiments. (B) Representative blots and quantification of immunoblot analyses using H4-specific antibodies on whole-cell extracts from WT and H2A-S129E mutant cells before and after Zeocin treatment. Dpm1 was used as a loading control. Immunoblot quantification of H4 signal intensity relative to that of the loading control (ctrl) was performed using ImageJ and is shown as mean \pm s.d. of five experiments. (C) Top: representative image of SPB and CenIV fluorescence imaging (dotted line outlines the cell). Bottom: cumulative distribution function (CDF) plot of SPB-CenIV 2D distances in WT and H2A-S129E mutant cell populations treated or not with Zeocin, as indicated. Three independent experiments were performed. The total number of cells analyzed is as follows: WT, $n=1543$; WT+Zeo, $n=973$; H2A-S129E, $n=1178$; H2A-S129E+Zeo, $n=1081$. (D) Bar plots show 2D intrachromosomal distances in untreated WT (blue) and H2A-S129E (cyan) cells, and in Zeocin-treated WT (red) and H2A-S129E (magenta) cells, for each of the four pairs of green-red labeled loci in P1-P4 strains. The horizontal line at the center of each box indicates the median value (shown in each box); the bottom and top limits of each box indicate the lower and upper quartiles, respectively. The whiskers indicate the full range of measured values, except for outliers (calculated by MATLAB plot function), which are shown as small red '+' symbols. Number of analyzed cells (n) is indicated. *** $P \leq 0.001$; ** $P \leq 0.01$; * $P \leq 0.05$; n.s., not significant (Wilcoxon rank sum test).

$\Delta rad9$ H2A-S129E double mutant and $P=4.4 \times 10^{-14}$ between WT and $\Delta rad9$, as determined by a contingency chi-square test; Fig. 2A and Fig. 3C). Surprisingly, Rad53 phosphorylation was not restored

in the $\Delta rad9$, H2A-S129E double mutant (Fig. 3C). Thus, the failure of the $\Delta rad9$ mutant to survive and activate cell cycle arrest in response to Zeocin is rescued by the H2A-S129E mutation

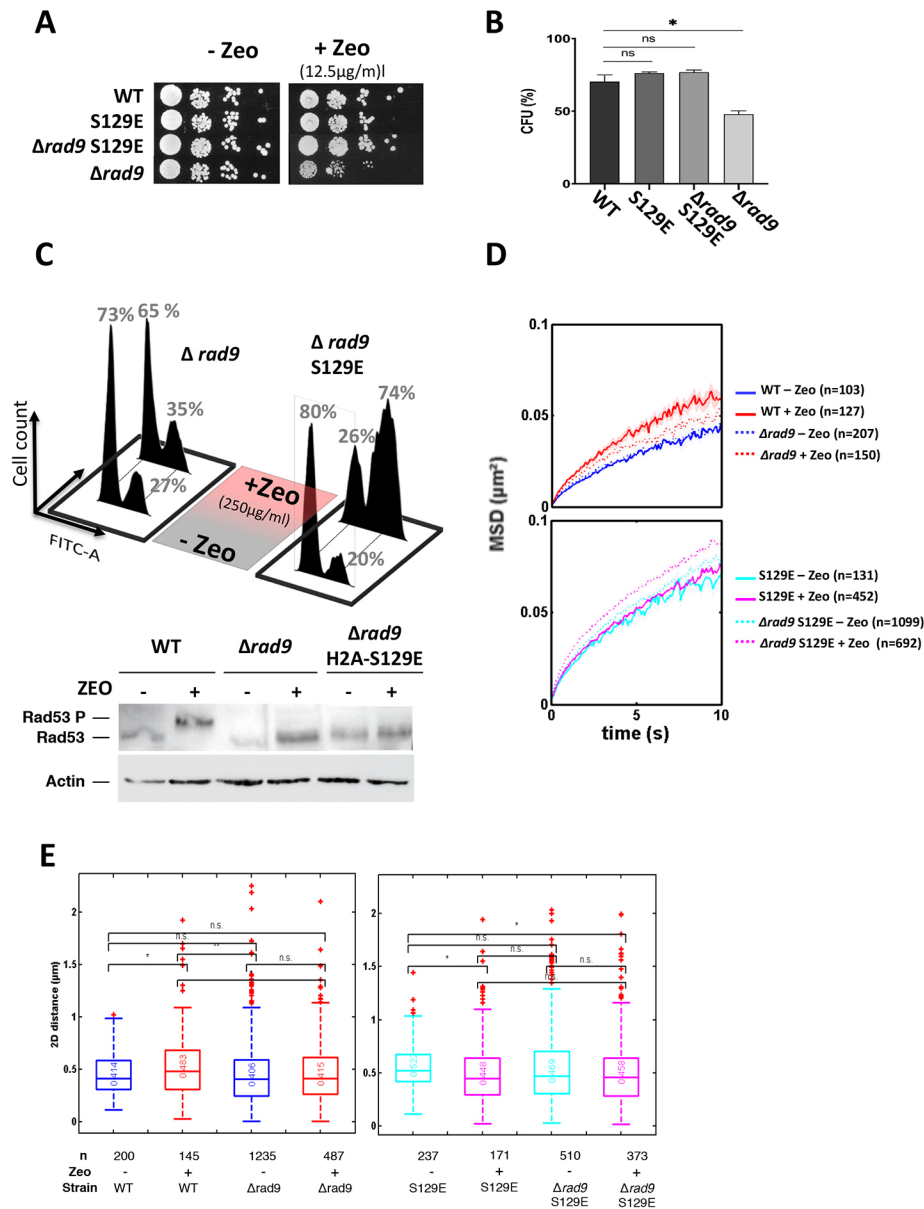


Fig. 3. The H2A-S129E mutant suppresses Rad9 checkpoint control of cell survival, global chromatin dynamics and intrachromosomal distances upon Zeocin treatment. (A) Drop assay (left to right, tenfold dilutions) of WT, $\Delta rad9$ and $\Delta rad9$ H2A-S129E double mutant cells in the absence (-Zeocin) and the presence (+Zeocin) of 12.5 $\mu\text{g/ml}$ Zeocin for the P3 strain. The single H2A-S129E mutant is also shown. (B) Colony forming units (CFU) calculated as the percentage of grown colonies in the presence Zeocin relative to grown colonies in the absence of Zeocin, after spreading of ~200 colonies for each condition for WT, H2A-S129E mutant, $\Delta rad9$ mutant and $\Delta rad9$ H2A-S129E double mutant cells. Data are presented as mean \pm s.d. from three independent experiments. * $P \leq 0.05$; n.s., not significant (non-parametric t -test). (C) Top: flow cytometry analysis of the cell cycle in the indicated strains in the absence or the presence of 250 $\mu\text{g/ml}$ Zeocin, as described in Fig. 2A. The percentage of cells in the low and high FITC-A populations are indicated, based on three experiments. Bottom: representative results from immunoblotting showing the phosphorylation (P) status of Rad53-HA in WT, $\Delta rad9$ and $\Delta rad9$ H2A-S129E cells in response to Zeocin treatment. Actin was used as a loading control. Blots are representative of five experiments. (D) Mean square displacements (MSDs), calculated as in Fig. 1., for WT compared to $\Delta rad9$ (top) and H2A-S129E compared to $\Delta rad9$ H2A-S129E double mutant (bottom). Data are presented as the cell population mean \pm s.e.m. The numbers of cells used to calculate each curve (n) are indicated. (E) Box plots show 2D intrachromosomal distances of untreated and Zeocin-treated cells (as indicated) for WT and $\Delta rad9$ (left) and for H2A-S129E and the double mutant $\Delta rad9$ H2A-S129E (right). The horizontal line at the center of each box indicates the median value (shown in each box); the bottom and top limits of each box indicate the lower and upper quartiles, respectively. The whiskers indicate the full range of measured values, except for outliers, which are shown as small red '+' symbols, as in Fig. 1. Number of analyzed cells (n) is indicated and ranges from 150 to ~1200. * $P \leq 0.05$; ** $P \leq 0.01$; n.s., not significant (non-parametric t -test).

independently of Rad53 phosphorylation. These results suggest that an early DDR response in the phosphomimetic H2A-S129E mutant enables cells to repair damage by circumventing the absence of Rad9 (see Discussion).

We then measured global chromatin mobility in these mutants in the absence and the presence of Zeocin (Fig. 3D). Whereas the $\Delta rad9$

mutant behaved similarly to WT in undamaged conditions, the absence of *RAD9* partially impeded the enhancement of global chromatin mobility observed in WT strains upon DNA damage, in agreement with the findings of Seeber et al. (2013). Interestingly, in both undamaged and damaged conditions, the $\Delta rad9$ H2A-S129E double mutation induced a massive increase in global dynamics,

comparable to that observed for the single H2A-S129E mutant (Fig. 3D; Fig. S3B). To check whether changes in chromosome dynamics also translate into chromatin structural changes in the $\Delta rad9$ H2A-S129E double mutant, we also measured intrachromosomal 2D distances (Fig. 3E). We confirmed that in the absence of Zeocin treatment, the distances in the $\Delta rad9$ mutant were not significantly different from those of the wild-type strain and that the distances in the $\Delta rad9$ H2A-S129E double mutant were comparable to those in the single H2A-S129E mutant. As expected from the dynamic behavior, in the presence of Zeocin, $\Delta rad9$ caused a modest increase in intrachromosomal distances as compared to those in the WT, but increased as much as H2A-S129E in the double $\Delta rad9$ H2A-S129E mutant (Fig. 3E). Thus, the structural changes induced by the H2A-S129E mutant in the $\Delta rad9$ background corroborate the observations of the chromosomal dynamics. Our results highlight the capacity of the H2A-S129E mutation to suppress the specific contribution of Rad9 to cell survival, DNA damage checkpoint and global chromosome dynamics when the genome is damaged, possibly through chromatin structure modification.

Mimicking H2A-S129 phosphorylation increases NHEJ and reduces translocation rates of the $\Delta rad9$ mutant

As the drop test and CFU assays showed no difference between survival of WT and H2A-S129E strains, and because the H2A-S129E mutation restored survival of $\Delta rad9$ mutants, we asked whether the H2A-S129E mutation facilitates DSB repair. We chose to study NHEJ repair because chromosome mobility could be a means for promoting the joining of double-stranded extremities (Dimitrova et al., 2008; Lottersberger et al., 2015; Ma et al., 2021). We investigated the effect of both $\Delta rad9$ and H2AS129E mutations on the NHEJ repair pathway by using a plasmid repair assay, in which repair of a linear plasmid can only be mediated by NHEJ. We generated linear plasmids with cohesive ends by cutting a *HIS3*-containing centromeric plasmid using *EcoRI* enzyme. In this assay, only circularized plasmids confer histidine prototrophy to the transformed cells. A $\Delta yku70$ mutant, which is impaired in NHEJ, was used as a control for plasmid linearization. After transformation with the digested plasmids, His⁺ colonies were obtained in the $\Delta yku70$ mutant at 10-fold lower frequency than in WT cells. These data indicate that most transforming molecules were efficiently re-circularized in WT (Fig. 4A). The number of His⁺ colonies recovered in the H2A-S129A mutant was almost as low as in the $\Delta yku70$ mutant, revealing that plasmid circularization by NHEJ is compromised in the absence of γ -H2A. This result is consistent with previous studies showing that truncated forms of H2A lacking S129 are deficient for NHEJ, and is also consistent with an increased resection rate previously observed in the H2A-S129A mutant (Downs et al., 2000; Eapen et al., 2012; Moore et al., 2007). In contrast, the number of His⁺ colonies was ~1.3 times higher in the H2A-S129E mutant than in WT, indicating that mimicking H2A phosphorylation allowed more effective repair by NHEJ than in WT (Fig. 4B). In the $\Delta rad9$ mutant, the number of His⁺ cells was 4 to 8 times lower than in the WT (Fig. 4B), an expected result given the role of Rad9 in limiting 5' DNA end resection (Ferrari et al., 2015). Remarkably, the number of His⁺ colonies was similar to WT in the $\Delta rad9$, H2A-S129E double mutant. Thus, the restoration of cell survival following DNA damage observed in the $\Delta rad9$ H2A-S129E double mutant could be linked to an increase in NHEJ efficiency. In turn, increased chromosome motion observed in H2A-S129E mutants could promote NHEJ, as has been observed for dysfunctional telomeres in mammalian cells (Dimitrova et al., 2008; Lottersberger et al., 2015).

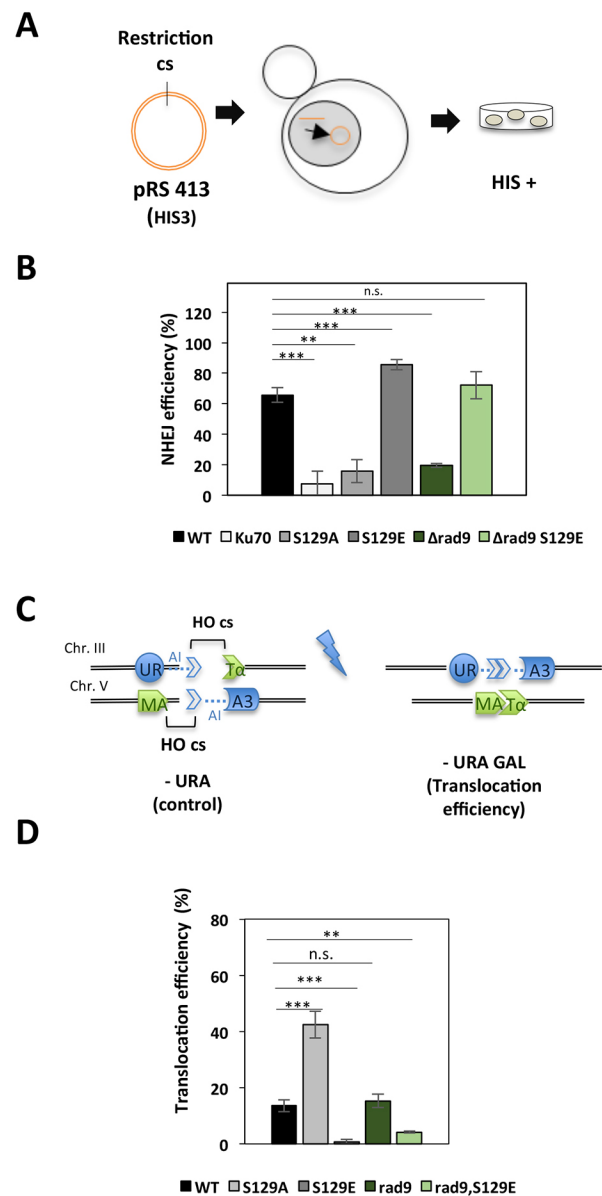


Fig. 4. Mimicking H2A S129 phosphorylation increases NHEJ and decreases translocation rates. (A) Schematic of the NHEJ assay principle. A replicative plasmid carrying *HIS3* as an auxotrophic marker (pRS413) is linearized by *EcoRI* enzyme (cs, cut site) and used for yeast transformation. In strains with efficient NHEJ, plasmid extremities are joined (arrow) and His⁺ colonies are recovered on plates lacking histidine. (B) Rejoining efficiency was calculated for the indicated strains as the percentage recovery of His⁺ colonies after transformation of a linearized plasmid, relative to recovery following introduction of a non-linearized plasmid. A $\Delta yku70$ mutant (Ku70) is impaired in NHEJ, and was used as a control for plasmid digestion efficiency. The bar graph shows the mean \pm s.e.m. of five experiments. ** $P \leq 0.01$; *** $P \leq 0.0001$; n.s., not significant (non-parametric *t*-test). (C) Schematic of the strain used to measure translocation. Two DSBs generated by HO endonuclease (HO cs), an intronic sequence (dotted line) and truncated forms of *URA3* are depicted on two distinct chromosomes (Chr. III and Chr. V). Reciprocal end-joining produces Ura⁺ cells. Al, artificial intron. (D) Percentage translocation efficiency for the indicated strains was calculated as the ratio of the number of Ura⁺ colonies recovered after persistent induction of DSBs (on -URA plates containing galactose) relative to the number recovered in non-translocated conditions (+URA plates containing galactose). The bar graph shows the mean \pm s.d. of five experiments. ** $P \leq 0.01$; *** $P \leq 0.0001$; n.s., not significant (non-parametric *t*-test).

In addition to efficient repair of a single DSB by NHEJ, increased mobility in mammals has been proposed to counteract ectopic repair when DSBs are rare (Lotterberger et al., 2015). We therefore analyzed the effect of large-scale chromatin mobility in the H2A-S129E mutant on translocation rates. To test for this, we used a genetic system in which recovery of Ura⁺ *MATa* colonies is mediated by a reciprocal translocation between two DSBs generated in truncated *URA3* on two distinct chromosomes, chromosomes III and V (Lee et al., 2008; Fig. 4C). DSBs were induced by expressing the HO endonuclease from the galactose-inducible *GAL1-10* promoter. We first checked by qPCR that the cutting efficiency was similar after 1 h of galactose induction at the two HO cutting sites in WT and H2A-S129E mutant cells (Fig. S4). Then, translocation rates were measured after permanent induction of HO on galactose-containing plates. We plated cells directly onto galactose-containing media, supplemented with or without uracil. The rate of translocation was calculated by counting the number of Ura⁺ survivors divided by the total amount of survivors grown on non-selective plates for each strain. Whereas the phospho-deficient H2A-S129A mutation increased translocation rates ~3-fold compared to those in WT (13.5%±2.6 and 42.4%±4.8 for WT and H2A-S129A, respectively; mean±s.d.), as previously documented (Fig. 4D; Lee et al., 2008), the H2A-S129E mutation decreased translocation rates by ~13-fold (1.1%±0.6%; Fig. 4D). As expected, the efficiency of translocation in the mutant *Δrad9* was comparable to that of WT (Fig. 4D; Lee et al., 2008) and was significantly reduced in the double mutant *Δrad9* H2A-S129E (Fig. 4D).

Taken together, our results indicate that H2A phosphorylation mimics an increase in chromosomal dynamics favorable to a local NHEJ repair concomitant with a sharp decrease in the interchromosomal translocation rate.

DISCUSSION

Here, we show that in the absence of DNA damage induction, the H2A-S129E mutation fully recapitulates global chromosome and chromatin dynamics previously observed upon Zeocin treatment (Hauer et al., 2017; Herbert et al., 2017). The specific effect of the H2A-S129E mutation is to mimic H2A phosphorylation, as previously assessed against the criterion of being recognized by an anti- γ -H2AX antibody (Eapen et al., 2012). One intriguing consequence of the H2A-S129E mutation is the bypassing of an essential function of the DNA damage checkpoint protein, Rad9, when Zeocin is present. Locus tracking in living cells revealed that the H2A-S129E mutation restores the high chromatin mobility induced by DNA damage, which is defective in *Δrad9*. This likely indicates the importance of global mobility and/or chromatin structure for the early checkpoint. Because the γ -H2A(X) modification is not necessary to set up the checkpoint, but is required to maintain it and facilitate access by repair proteins (Celeste et al., 2003; Dotiwala et al., 2010; Kruhlak et al., 2006), the structural modification of chromatin at the break site may serve as the first sensor signal (Bakkenist and Kastan, 2003; Burgess et al., 2014). Accordingly, we found that the enhanced global dynamics observed in the H2A-S129E mutant were not related to tethering of the centromeres, histone depletion or downstream checkpoints – mechanisms previously proposed to explain the increase in overall chromosome mobility detected when the genome is damaged (Lawrimore et al., 2017; Seeber et al., 2013; Smith et al., 2018; Strecker et al., 2016). Rather, we found that the negative charges of glutamic acid (but not the uncharged alanine) enhanced global dynamics together with increased intrachromosomal distances. These two characteristics indicate a structural modification of the

chromatin compatible with its stiffening (Herbert et al., 2017). If transcription of some key regulators involved in the DDR was modified in H2A-S129E-mutated cells, a similar phenotype could be expected. However, no such changes in transcription could be detected by RNAseq analyses of the H2A-S129E mutant (S. Bohn, B.L., J.E.H. and N. Krogan, unpublished result). The fact that *Δrad9* DNA damage sensitivity and checkpoint defects were rescued by H2A-S129E suggests that H2A-S129E may have a positive effect on repair and genome stability. We tested this proposal by examining the repair by NHEJ of a linearized plasmid and found that it was favored in H2A-S129E cells. In addition, the direct measurement of DSB translocations revealed that the level of interchromosomal end joining was severely reduced in H2A-S129E mutants. These observations are consistent with the idea that increased mobility of DNA extremities may favor their joining and repair. Conversely, it limits repair between two DSBs *in trans*, as has been suggested to happen in mammalian cells under physiological conditions (Lotterberger et al., 2015). We propose that changes in chromosomal conformation due to H2A phosphorylation are a means to efficiently modulate the DDR.

A model for regulation of the DDR by changes in chromatin structure

Chromatin structure is one of the key factors in the DDR, because it is the first to be altered both by the damage that generates the DSB and by the accumulation of histone modifications and repair proteins at the damaged site. A DSB might alter topological constraints on the chromatin fiber, although little is known about these constraints associated with higher-order chromosome organization (Canela et al., 2017). Histone posttranslational modifications on the other hand, such as phosphorylation of H2A, which can extend from the DSB over areas as large as 50 kb on either side of the DSB (Lee et al., 2014; Shroff et al., 2004), also change the chromatin structure, the repulsive negative charges due to phosphorylation being compatible with a stiffer chromatin (Celeste et al., 2003; Herbert et al., 2017; Lee et al., 2008; Miné-Hattab et al., 2017; Reina-San-Martin et al., 2003). Normally, γ -H2A(X) modifications occur around the site of a DSB, which exhibits enhanced local motion, while inducing global mobility changes in undamaged regions. Here, we observed that in the absence of damage, the whole H2A-S129E-containing chromatin displayed enhanced mobility; however, we cannot yet determine whether the enhanced global mobility seen in WT strains after Zeocin treatment represents global motion or is a manifestation of a local motion.

In mammals, regulation of the ATM response by chromatin structure has also been proposed to contribute to the extremely rapid and sensitive response to damage across the nucleus, as shown by ATM activation in the absence of detectable damage during hypotonic shock or during histone deacetylation (Bakkenist and Kastan, 2003; Kumar et al., 2014). The changes in chromatin mobility that we report here, where no damage was induced, were systematically accompanied by an increase in distances between the arrays along the chromosome, a parameter that can be explained by a change in chromatin structure (Amitai et al., 2017; Arbona et al., 2017; Hauer et al., 2017; Herbert et al., 2017). The higher-order chromatin structure modification due to H2A-S129E mutation has previously been proposed to correspond to a decreased compaction (Downs et al., 2000), in agreement with a more relaxed profile of 2 μ plasmid from H2A-S129E-containing cells and a faster digestion of the H2A-S129E chromatin by micrococcal nuclease (Downs et al., 2000). The fact that in the H2A-S129E mutant, the protection

pattern or the length of nucleosomal repeats is conserved (Downs et al., 2000), is also compatible with a stiffer chromatin, but the number of nucleosomes per length unit (i.e. compaction) remains to be determined. Similarly, treatment with Zeocin has been shown to cause nucleosome loss, as documented by degradation of histones H3 and H4 (Hauer et al., 2017). Histone degradation could explain the additional modest effect on mobility and intrachromosomal distances observed in the H2A-S129E mutant when treated with Zeocin, because the global level of H4 was not affected in undamaged H2A-S129E cells, but substantial degradation was observed in both WT and H2A-S129E cells in the presence of Zeocin. Thus, chromatin stiffening due to H2A phosphorylation and chromatin decompaction due to histone loss could exist together in Zeocin-treated cells. Only close examination of the chromatin structure by super-resolution microscopy will help to determine the nature of these chromatin changes.

Our live-cell chromosome dynamics observations combined with the genetic evidence presented here suggest a novel mode of DDR regulation via an extremely efficient modification of the chromosome structure. The activation of the DDR was evident after DNA damage, which restored cell cycle arrest in the double mutant $\Delta rad9$, H2A-S129E. Which effectors could be responsible for the reactivation of the checkpoint? It was tempting to test whether the phosphorylation of Rad53 was restored under these conditions. The lack of detectable phosphorylated Rad53 indicates that downstream checkpoint activation occurs through other effectors that have yet to be identified. Another hypothesis is linked to the Mad2-mediated spindle assembly checkpoint (SAC), which is necessary to sustain arrest (Dotiwala et al., 2010). Activation of this extended G2/M arrest is dependent on formation of γ -H2A (Dotiwala et al., 2010). A possible explanation for the bypassing of the effects of $\Delta rad9$ by the H2A-S129E mutation could be an extended arrest through the Mad2 SAC. Regardless of the nature of the effectors activated by H2A-S129E, our results indicate that H2A posttranslational modification of chromatin, which can be achieved in the absence of any protein synthesis, results in a very proficient DDR, probably faster than any transcriptional regulation.

What is the function of H2A-S129E?

In the presence of H2A-S129E, Rad9 is no longer essential for arresting cells in G2/M after DNA damage or for facilitating damage-associated chromosome mobility. Based on the evidence presented here, we propose that chromosome mobility induced by chromatin structural changes is an efficient way to signal the presence of damage and to assist repair. The chromatin changes and the enhanced dynamics may favor accessibility of the NHEJ repair machinery to the extremities of the break. In agreement with this, Tel1^{ATM}, which phosphorylates H2A-S129, facilitates NHEJ repair protein recruitment and prevents dissociation of broken DNA ends (Lee et al., 2008). Consequently, inappropriate rejoining of chromatin fragments, which can result in genetic translocations, is decreased, as we and others have observed both in yeast and mammals (Celeste et al., 2003; Lee et al., 2008; Reina-San-Martin et al., 2003). Besides, DSB end resection is thought to regulate the γ -H2A(X)-mediated recruitment of remodeling complexes, including SWR1, Fun30 and INO80, to promote repair by NHEJ and HR (Eapen et al., 2012; Horigome et al., 2014; van Attikum et al., 2007). Notably, the interaction between Fun30 and H2A-S129E chromatin is impaired, raising the possibility that resection factors in the H2A-S129E mutant would also be impaired, thus favoring NHEJ. The role of chromosome mobility in repair by NHEJ is consistent with the observation that increased roaming of deficient telomeres facilitates NHEJ in mammals (Dimitrova et al., 2008;

Lotterberger et al., 2015). Concerning translocations (i.e. the junction between two DSBs on distinct chromosomes), two theories are proposed. On one hand, the limited motion of DSB ends would have a greater probability of forming a translocation provided they are spatially close; on the other hand, mobile ends would favor the connection between ends that have lost their proper interaction. Thus, NHEJ made efficient thanks to the mobility of DSB extremities would counterbalance ectopic repair between two distant breaks. Our results favor this last hypothesis. Mobilization of DSBs to promote faithful repair may be preserved by evolution. The reason why such an H2A-S129E mutation has not been positively selected may be linked to the fact that it is useful to maintain a regulated mobility rather than an inherently increased one.

Finally, the evolutionary conservation of chromosome mobility suggests the possibility that similar mechanisms acting through chromatin modification exist in other organisms. In both yeast and mammals, the cellular surveillance machinery senses both DNA damage and concomitant changes in chromatin structure in order to activate DDR signaling. In mammalian cells, the response to DNA damage is complex and includes protein modifications that do not exist in yeast, such as poly(ADP-ribosylation) by poly(ADP-ribose) polymerases (PARPs). PARPs also induce chromatin mobility (Sellou et al., 2016; Smith et al., 2019). It would be interesting to test whether chromatin mobility induced by PARylation in mammalian cell lines helps to preserve chromatin integrity.

MATERIALS AND METHODS

Strain construction

All strains, plasmids and primers used in this study are listed in Table S1. Fluorescently labeled strains used in this study were constructed by insertion of Tet operator (*tetO*) and Lac operator (*lacO*) arrays inserted at specific locations on chromosome IV (Robinett et al., 1996). These arrays are bound by Tet repressor (TetR) and Lac inducer (LacI), which were fused to the fluorescent proteins mRFP and eGFP, respectively.

Yeast H2A-S129A and H2A-S129E mutants were constructed using CRISPR/Cas9 technology, as described by Anand et al. (2017). Briefly, a 20 nucleotide sequence corresponding to the sgRNA, flanked by a NGG sequence (Cas9 PAM), was selected from the sequence of both H2A genes (*HTA1* and *HTA2*) encoding serine 129. A complementary sequence was designed to form a duplex with *BpII* overhangs and cloned into *BpII*-digested yeast Cas9 plasmid (pEF562; 1:1). To introduce the modifications into the yeast genome, a single-stranded 80 nucleotide donor sequence was designed, consisting of 40 nucleotides upstream and 40 nucleotides downstream of the targeted sequence and containing an alanine 129 (H2A-S129A) or glutamic acid 129 (H2A-S129E) codon instead of the serine 129. Yeast cells were transformed with 1 μ g yeast Cas9 plasmid containing the sgRNA against either *HTA1* or *HTA2* (pEF567 and pEF568, respectively) and 2 μ g donor sequence. After transformation, the Cas9 plasmids were lost, and sequence modifications of the *HTA1* and *HTA2* genes were verified by sequencing. Yeast strain YEF1375 corresponds to yeast strain yKD1866 (from Karine Dubrana, François Jacob Institute of Biology, CEA, France) and SLY60 (from Sang Eun Lee, Department of Molecular Medicine and Institute of Biotechnology, San Antonio, Texas, USA).

Yeast cell cultures for fluorescence microscopy observations

Yeast cells were grown in a selective medium [SC; 0.67% yeast nitrogen base without amino acids (Difco), supplemented with a mix of amino acids (Sigma Aldrich) lacking uracil, and 2% glucose (Sigma Aldrich)] overnight at 30°C, diluted 1:50 in the morning and grown for two generations. Where relevant, Zeocin at a concentration of 250 μ g/ml was added to the culture 6 h before imaging. Cells reaching exponential phase (1 OD at 600 nm) were then centrifuged, concentrated to 1.5×10^7 cells/ml, and 3 μ l was spread on agarose patches [SC containing 2% agarose (Euromedex)]. Patches were sealed using VaLaP (1/3 vaseline, 1/3 lanoline, and 1/3 paraffin).

Wide-field microscopy

Live-cell imaging was performed using a wide-field microscopy system featuring a Nikon Ti-E body equipped with the Perfect Focus System and a 60× oil immersion objective with a numerical aperture of 1.4 (Nikon, Plan APO). We used an Andor Neo sCMOS camera, which features a large field of view of 276×233 μm at a pixel size of 108 nm. We acquired 3D z-stacks consisting of 35 frames with z-steps of 300 nm using a dual-band filter set (eGFP, mRFP). For each z position, two color channels were consecutively acquired with an exposure time of 100 ms. The complete imaging system, including camera, piezo stage and LEDs (SpectraX) was controlled by the NIS-elements software. Original microscopy data (movies and z-stacks) are available upon request.

Wide-field image analysis and statistics

Image analyses were performed using Fiji (<https://imagej.net/Fiji>) plugins. Briefly, images were corrected for chromatic aberrations using the plugin 'Descriptor-based registration (2d/3d)'. Once correction was applied to all acquired images, the 'Detect ROI' script allowed automatic selection of non-dividing cells and computation of the *x-y* coordinates of the red and green loci using a custom-made Fiji plugin implementing Gaussian fitting. For tracking in time-lapse microscopy, we used the same custom-written Fiji plugin, which allowed extraction of locus positions over the entire timecourse for each nucleus. A custom-made MATLAB script that corrected global displacements and computed MSD curves for each trajectory using non-overlapping time further analyzed these trajectories. Finally, other MATLAB scripts were used to fit power laws to individual MSD curves or population-averaged MSDs over time intervals 0.1–10 s.

Colony forming unit assay

Each strain was grown overnight in 3 ml of YPD [YPD; 1% bacto peptone (Difco), 1% bacto yeast extract (BD) and 2% glucose (Sigma)]. The day after, each culture was appropriately diluted and ~200 colonies were plated onto YPD plates and YPD plates supplemented with Zeocin at a concentration of 12.5 μg/ml in order to induce random DSBs (as described in Seeber et al., 2013). Colonies were counted after 2–3 days of incubation at 30°C. For each strain, three independent experiments were performed with the corresponding controls.

Plasmid repair assay

The plasmid pRS413 (*HIS3*; Addgene) was linearized with *EcoRI*, which generates cohesive ends. Equal numbers of competent cells are transformed with 100 ng of either linear or circular plasmids. Following transformation with linear plasmid, the cell must repair the *HIS3*-containing plasmid to survive subsequent plating on dropout plates lacking histidine [SC; 0.67% yeast nitrogen base without amino acids (Difco), supplemented with a mix of amino acids (Sigma Aldrich) lacking histidine, 2% glucose (Sigma Aldrich) and 2% Bacto Agar (BD)]. Each strain's repair efficiency was quantified, relative to the isogenic wild type, by assessing the number of colonies obtained with the cut plasmid relative to the circular plasmid. Each mutant was assayed a minimum of three times in triplicate, and the averaged results, standard errors and results of unpaired *t*-tests are reported.

Translocation assay

Strains were grown overnight in 20 ml of synthetic minimum medium SC [2% raffinose, 0.67% yeast nitrogen base without amino acids (Difco), supplemented with a mix of amino acids (Sigma Aldrich)] at 30°C, diluted to a density corresponding to an OD of 0.2 at 600 nm, and grown for 3 h in the same synthetic minimal medium in order to reach exponential growth phase (OD=1). Cultures were diluted appropriately to have ~10⁴ and ~10³ colonies/plate after counting with a Malassez chamber, then were plated onto galactose-containing SC dishes with or without uracil. Colonies were counted after 2–3 days of incubation at 30°C. Translocation efficiency (%) was determined by calculating the ratio between the number of colonies in SC plates lacking uracil and containing galactose and the number of colonies in non-selective SC plates containing galactose. For each strain, three independent experiments were performed.

FACS analyses

Cells were grown to mid-log phase in liquid YPD medium cultures, and treated or not with Zeocin at 250 mg/μl for 6 h at 30°C. After incubation, samples were fixed in 70% ethanol and kept at 4°C for 48 h. Cells were then resuspended in 50 mM sodium citrate (pH 7) containing RNaseA at 0.2 mg/ml final concentration. After incubation at 37°C for 1 h, Sytox Green was added to a final concentration of 1 mM. A total of 10⁶ cells were analyzed with a CANTO II flow cytometer (BD Biosciences). Aggregates and dead cells were gated out, and percentages of cells with 1C and 2C DNA content were calculated using FLOWJO software.

Western blotting

Cells were grown to mid-log phase in liquid YPD medium cultures and then treated with Zeocin at 250 mg/μl for 3 h at 30°C. After incubation, samples were washed once with water and resuspended in 20% trichloroacetic acid. Cells were lysed by sonication three times for 30 s, and the protein lysates were pelleted by centrifugation at 24,104 *g* for 5 min at 4°C. The pellets were dissolved in 1× SDS sample loading buffer by boiling for 5 min. Samples were centrifuged for 30 s at 18,000 *g* in a microcentrifuge, and the supernatant was retained as the protein extract. Protein samples were resolved on a Bolt 10% Bis-Tris Plus gel (Thermo Fisher Scientific; NW00100BOX) and transferred onto a polyvinylidene difluoride membrane (Immobilon-P; Millipore). Membranes were probed with anti-H4 (1:5000; ab10158; Abcam) and anti-HA-HRP (1:1000; 26183-HRP; Thermo Fisher Scientific) antibodies. As a loading reference, we used anti-Dpm1 (1:2000; 5C5A7; Thermo Fisher Scientific) and anti-actin antibodies (1:1000; MA1-744; Merck). Anti-mouse IgG and anti-rabbit IgG HRP-conjugated secondary antibodies were obtained from Thermo Fisher Scientific (A11005 and A31556). Blots were developed using the ECLplus western blotting system (GE Healthcare).

Acknowledgements

We thank S. Eun Lee and K. Dubrana for strains and advice, S. Duchez for her help with the FACS experiments and A. Carré Simons for drop tests. We acknowledge P. Lesage, A. Bonnet, P. Therizols, A. Canat and D. Waterman for their helpful comments on the manuscript. The authors would also like to thank their respective team members for very fruitful discussions.

Competing interests

The authors declare no competing or financial interests.

Author contributions

Conceptualization: F.G.F., E.F.; Methodology: F.G.F., B.L., R.B., E.F.; Software: Y.K.; Validation: F.G.F., E.F.; Formal analysis: F.G.F., Y.K., R.B.; Investigation: F.G.F., R.B.; Resources: J.E.H., E.F.; Data curation: F.G.F., Y.K., E.F.; Writing - original draft: E.F.; Writing - review & editing: F.G.F., J.E.H., E.F.; Visualization: E.F.; Supervision: E.F.; Project administration: E.F.; Funding acquisition: E.F.

Funding

This work was supported by Labex 'Who am I?' (ANR-11-LABX-0071, IdEx ANR-11-IDEX-0005-02). E.F. has support from Agence Nationale de la Recherche (ANR-13-BSV8-0013-01), IDEX SLI (DXCAIUHSLI-EF14) and Cancéropôle Ile de France (ORFOCRISE PME-2015). Y.K. and E.F. acknowledge the support of Fondation pour la Recherche Médicale (ING20160435205). F.G.F. acknowledges the Peruvian Scholarship Científica of Consejo Nacional de Ciencia, Tecnología e Innovación Tecnológica (CONCYTEC) for supporting her PhD study at INSERM and Diderot University and support by Fondation ARC pour la Recherche sur le Cancer (DOC20190508798). J.E.H. has a grant support from the National Institutes of Health (R35 127029). B.L. was supported by a National Institute of General Medical Sciences Genetics Training Grant (T32GM007122). This study contributes to the IdEx Université de Paris (ANR-18-IDEX-0001). Deposited in PMC for release after 12 months.

Supplementary information

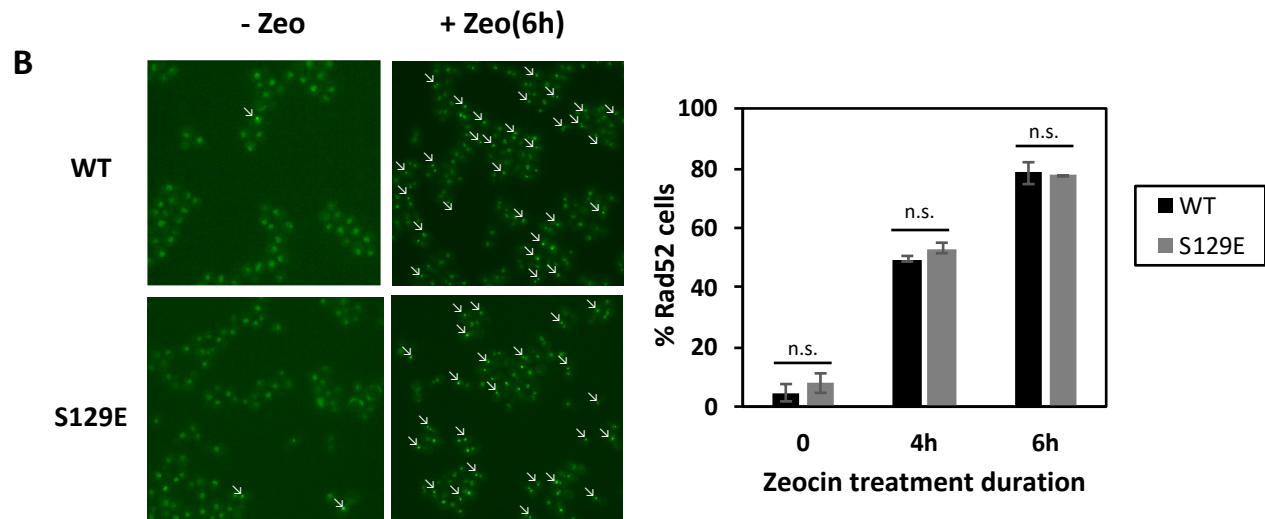
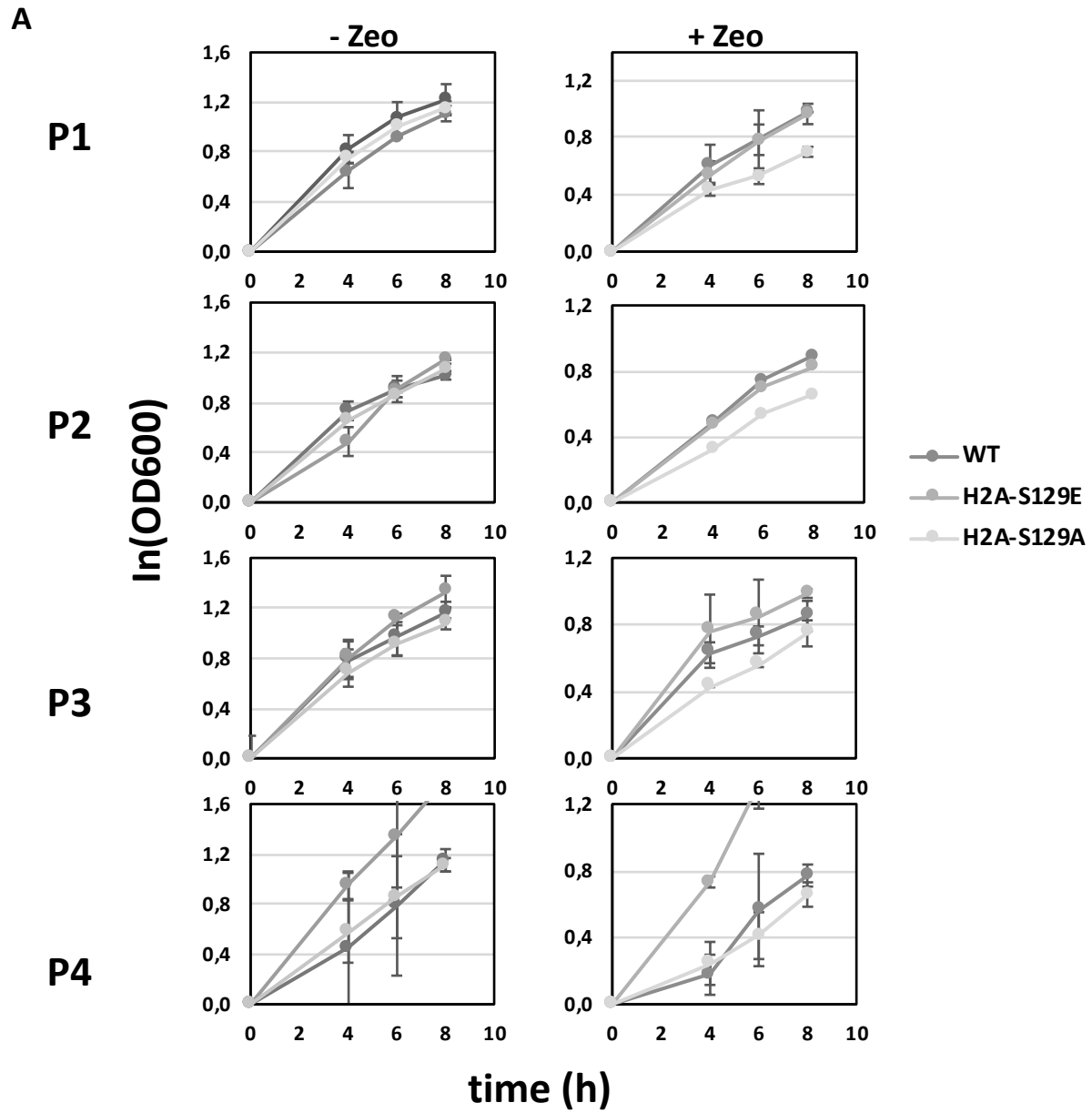
Supplementary information available online at <https://jcs.biologists.org/lookup/doi/10.1242/jcs.258500.supplemental>

References

Amitai, A., Seeber, A., Gasser, S. M. and Holcman, D. (2017). Visualization of chromatin decompaction and break site extrusion as predicted by statistical polymer modeling of single-locus trajectories. *Cell Rep.* **18**, 1200-1214. doi:10.1016/j.celrep.2017.01.018

- Anand, R., Beach, A., Li, K. and Haber, J. (2017). Rad51-mediated double-strand break repair and mismatch correction of divergent substrates. *Nature* **544**, 377–380. doi:10.1038/nature22046
- Arbona, J.-M., Herbert, S., Fabre, E. and Zimmer, C. (2017). Inferring the physical properties of yeast chromatin through bayesian analysis of whole nucleus simulations. *Genome Biol.* **18**, 81. doi:10.1186/s13059-017-1199-x
- Aylon, Y. and Kupiec, M. (2004). DSB repair: the yeast paradigm. *DNA Repair* **3**, 797–815. doi:10.1016/j.dnarep.2004.04.013
- Bakkenist, C. J. and Kastan, M. B. (2003). DNA damage activates ATM through intermolecular autophosphorylation and dimer dissociation. *Nature* **421**, 499–506. doi:10.1038/nature01368
- Bermejo, R., Capra, T., Jossen, R., Colosio, A., Frattini, C., Carotenuto, W., Cocito, A., Doksani, Y., Klein, H., Gómez-González, B. et al. (2011). The replication checkpoint protects fork stability by releasing transcribed genes from nuclear pores. *Cell* **146**, 233–246. doi:10.1016/j.cell.2011.06.033
- Bétermier, M., Bertrand, P. and Lopez, B. S. (2014). Is non-homologous end-joining really an inherently error-prone process? *PLoS Genet.* **10**, e1004086. doi:10.1371/journal.pgen.1004086
- Blankley, R. T. and Lydall, D. (2004). A domain of Rad9 specifically required for activation of Chk1 in budding yeast. *J. Cell Sci.* **117**, 601–608. doi:10.1242/jcs.00907
- Bonilla, C. Y., Melo, J. A. and Toczyski, D. P. (2008). Colocalization of sensors is sufficient to activate the DNA damage checkpoint in the absence of damage. *Mol. Cell* **30**, 267–276. doi:10.1016/j.molcel.2008.03.023
- Burgess, R. C., Burman, B., Kruhlak, M. J. and Misteli, T. (2014). Activation of DNA damage response signaling by condensed chromatin. *Cell Rep.* **9**, 1703–1717. doi:10.1016/j.celrep.2014.10.060
- Burma, S., Chen, B. P., Murphy, M., Kurimasa, A. and Chen, D. J. (2001). ATM phosphorylates histone H2AX in response to DNA double-strand breaks. *J. Biol. Chem.* **276**, 42462–42467. doi:10.1074/jbc.C100466200
- Canela, A., Maman, Y., Jung, S., Wong, N., Callen, E., Day, A., Kieffer-Kwon, K.-R., Pekowska, A., Zhang, H., Rao, S. S. P. et al. (2017). Genome organization drives chromosome fragility. *Cell* **170**, 507–521.e18. doi:10.1016/j.cell.2017.06.034
- Ceccaldi, R., Rondinelli, B. and D'Andrea, A. D. (2016). Repair pathway choices and consequences at the double-strand break. *Trends Cell Biol.* **26**, 52–64. doi:10.1016/j.tcb.2015.07.009
- Celeste, A., Fernandez-Capetillo, O., Kruhlak, M. J., Pilch, D. R., Staudt, D. W., Lee, A., Bonner, R. F., Bonner, W. M. and Nussenzweig, A. (2003). Histone H2AX phosphorylation is dispensable for the initial recognition of DNA breaks. *Nat. Cell Biol.* **5**, 675–679. doi:10.1038/ncb1004
- Cheblal, A., Challa, K., Seeber, A., Shimada, K., Yoshida, H., Ferreira, H. C., Amitai, A. and Gasser, S. M. (2020). DNA damage-induced nucleosome depletion enhances homology search independently of local break movement. *Mol. Cell* **80**, 311–326.e4. doi:10.1016/j.molcel.2020.09.002
- Clouaire, T., Rocher, V., Lashgari, A., Arnould, C., Aguirrebengoa, M., Biernacka, A., Skrzypczak, M., Aymard, F., Fongang, B., Dojer, N. et al. (2018). Comprehensive mapping of histone modifications at DNA double-strand breaks deciphers repair pathway chromatin signatures. *Mol. Cell* **72**, 250–262.e6. doi:10.1016/j.molcel.2018.08.020
- Cui, Y. and Bustamante, C. (2000). Pulling a single chromatin fiber reveals the forces that maintain its higher-order structure. *Proc. Natl. Acad. Sci. USA* **97**, 127–132. doi:10.1073/pnas.97.1.127
- Dimitrova, N., Chen, Y.-C. M., Spector, D. L. and De Lange, T. (2008). 53BP1 promotes non-homologous end joining of telomeres by increasing chromatin mobility. *Nature* **456**, 524–528. doi:10.1038/nature07433
- Dion, V., Kalck, V., Horigome, C., Towbin, B. D. and Gasser, S. M. (2012). Increased mobility of double-strand breaks requires Mec1, Rad9 and the homologous recombination machinery. *Nat. Cell Biol.* **14**, 502–509. doi:10.1038/ncb2465
- Dotiwala, F., Harrison, J. C., Jain, S., Sugawara, N. and Haber, J. E. (2010). Mad2 prolongs DNA damage checkpoint arrest caused by a double-strand break via a centromere-dependent mechanism. *Curr. Biol.* **20**, 328–332. doi:10.1016/j.cub.2009.12.033
- Downs, J. A., Lowndes, N. F. and Jackson, S. P. (2000). A role for Saccharomyces cerevisiae histone H2A in DNA repair. *Nature* **408**, 1001–1004. doi:10.1038/35050000
- Eapen, V. V., Sugawara, N., Tsabar, M., Wu, W.-H. and Haber, J. E. (2012). The Saccharomyces cerevisiae chromatin remodeler Fun30 regulates DNA end resection and checkpoint deactivation. *Mol. Cell Biol.* **32**, 4727–4740. doi:10.1128/MCB.00566-12
- Emerson, C. H. and Bertuch, A. A. (2016). Consider the workhorse: nonhomologous end-joining in budding yeast. *Biochem. Cell Biol.* **94**, 396–406. doi:10.1139/bcb-2016-0001
- Ferrari, M., Dibitetto, D., De Gregorio, G., Eapen, V. V., Rawal, C. C., Lazzaro, F., Tsabar, M., Marini, F., Haber, J. E. and Pelliccioli, A. (2015). Functional interplay between the 53BP1-Ortholog Rad9 and the Mre11 complex regulates resection, end-tethering and repair of a double-strand break. *PLoS Genet.* **11**, e1004928. doi:10.1371/journal.pgen.1004928
- Finn, K., Lowndes, N. F. and Grenon, M. (2012). Eukaryotic DNA damage checkpoint activation in response to double-strand breaks. *Cell. Mol. Life Sci.* **69**, 1447–1473. doi:10.1007/s00018-011-0875-3
- Forey, R., Poveda, A., Sharma, S., Barthe, A., Padioleau, I., Renard, C., Lambert, R., Skrzypczak, M., Ginalski, K., Lengronne, A. et al. (2020). Mec1 is activated at the onset of normal S phase by low-dNTP pools impeding DNA replication. *Mol. Cell* **78**, 396–410.e4. doi:10.1016/j.molcel.2020.02.021
- Goldstein, M. and Kastan, M. B. (2015). The DNA damage response: implications for tumor responses to radiation and chemotherapy. *Annu. Rev. Med.* **66**, 129–143. doi:10.1146/annurev-med-081313-121208
- Haber, J. E. (2018). DNA repair: the search for homology. *BioEssays* **40**, 1700229. doi:10.1002/bies.201700229
- Hammett, A., Magill, C., Heierhorst, J. and Jackson, S. P. (2007). Rad9 BRCT domain interaction with phosphorylated H2AX regulates the G1 checkpoint in budding yeast. *EMBO Rep.* **8**, 851–857. doi:10.1038/sj.embor.7401036
- Harrison, J. C. and Haber, J. E. (2006). Surviving the breakup: the DNA damage checkpoint. *Annu. Rev. Genet.* **40**, 209–235. doi:10.1146/annurev.genet.40.051206.105231
- Hauer, M. H., Seeber, A., Singh, V., Thierry, R., Sack, R., Amitai, A., Kryzhanovska, M., Eglinger, J., Holcman, D., Owen-Hughes, T. et al. (2017). Histone degradation in response to DNA damage enhances chromatin dynamics and recombination rates. *Nat. Struct. Mol. Biol.* **24**, 99–107. doi:10.1038/nsmb.3347
- He, X., Asthana, S. and Sorger, P. K. (2000). Transient sister chromatid separation and elastic deformation of chromosomes during mitosis in budding yeast. *Cell* **101**, 763–775. doi:10.1016/S0092-8674(00)80888-0
- Herbert, S., Brion, A., Arbona, J.-M., Lelek, M., Veillet, A., Lelandais, B., Parmar, J., Fernández, F. G., Almayrac, E., Khalil, Y. et al. (2017). Chromatin stiffening underlies enhanced locus mobility after DNA damage in budding yeast. *EMBO J.* **36**, 2595–2608. doi:10.15252/embj.201695842
- Horigome, C., Oma, Y., Konishi, T., Schmid, R., Marcomini, I., Hauer, M. H., Dion, V., Harata, M. and Gasser, S. M. (2014). SWR1 and INO80 chromatin remodelers contribute to DNA double-strand break perinuclear anchorage site choice. *Mol. Cell* **55**, 626–639. doi:10.1016/j.molcel.2014.06.027
- Jackson, S. P. and Bartek, J. (2009). The DNA-damage response in human biology and disease. *Nature* **461**, 1071–1078. doi:10.1038/nature08467
- Khurana, S., Kruhlak, M. J., Kim, J., Tran, A. D., Liu, J., Nyswaner, K., Shi, L., Jaiwal, P., Sung, M.-H., Hakim, O. et al. (2014). A macrohistone variant links dynamic chromatin compaction to BRCA1-dependent genome maintenance. *Cell Rep.* **8**, 1049–1062. doi:10.1016/j.celrep.2014.07.024
- Kondo, T., Wakayama, T., Naiki, T., Matsumoto, K. and Sugimoto, K. (2001). Recruitment of Mec1 and Ddc1 checkpoint proteins to double-strand breaks through distinct mechanisms. *Science* **294**, 867–870. doi:10.1126/science.1063827
- Kruhlak, M. J., Celeste, A., Deltore, G., Fernandez-Capetillo, O., Müller, W. G., McNally, J. G., Bazett-Jones, D. P. and Nussenzweig, A. (2006). Changes in chromatin structure and mobility in living cells at sites of DNA double-strand breaks. *J. Cell Biol.* **172**, 823–834. doi:10.1083/jcb.200510015
- Kumar, A., Mazzanti, M., Mistrik, M., Kosar, M., Beznoussenko, G. V., Mironov, A. A., Garré, M., Parazzoli, D., Shivashankar, G. V., Scita, G. et al. (2014). ATR mediates a checkpoint at the nuclear envelope in response to mechanical stress. *Cell* **158**, 633–646. doi:10.1016/j.cell.2014.05.046
- Lancelot, N., Charier, G., Couprie, J., Duband-Goulet, I., Alpha-Bazin, B., Quémener, E., Ma, E., Marsolier-Kergoat, M.-C., Ropars, V., Charbonnier, J.-B. et al. (2007). The checkpoint Saccharomyces cerevisiae Rad9 protein contains a tandem tudor domain that recognizes DNA. *Nucleic Acids Res.* **35**, 5898–5912. doi:10.1093/nar/gkm607
- Lawrimore, J., Barry, T. M., Barry, R. M., York, A. C., Friedman, B., Cook, D. M., Akialis, K., Tyler, J., Vasquez, P., Yeh, E. et al. (2017). Microtubule dynamics drive enhanced chromatin motion and mobilize telomeres in response to DNA damage. *Mol. Biol. Cell* **28**, 1701–1711. doi:10.1091/mbc.e16-12-0846
- Lazzaro, F., Sapountzi, V., Granata, M., Pelliccioli, A., Vaze, M., Haber, J. E., Plevani, P., Lydall, D. and Muzi-Falconi, M. (2008). Histone methyltransferase Dot1 and Rad9 inhibit single-stranded DNA accumulation at DSBs and uncapped telomeres. *EMBO J.* **27**, 1502–1512. doi:10.1038/emboj.2008.81
- Lee, K., Zhang, Y. and Lee, S. E. (2008). Saccharomyces cerevisiae ATM orthologue suppresses break-induced chromosome translocations. *Nature* **454**, 543–546. doi:10.1038/nature07054
- Lee, C.-S., Lee, K., Legube, G. and Haber, J. E. (2014). Dynamics of yeast histone H2A and H2B phosphorylation in response to a double-strand break. *Nat. Struct. Mol. Biol.* **21**, 103–109. doi:10.1038/nsmb.2737
- Li, K., Bronk, G., Kondev, J. and Haber, J. E. (2020). Yeast ATM and ATR kinases use different mechanisms to spread histone H2A phosphorylation around a DNA double-strand break. *Proc. Natl. Acad. Sci. USA* **117**, 21354–21363. doi:10.1073/pnas.2002126117
- Lotterberger, F., Karssemeijer, R. A., Dimitrova, N. and De Lange, T. (2015). 53BP1 and the LINC complex promote microtubule-dependent DSB mobility and DNA repair. *Cell* **163**, 880–893. doi:10.1016/j.cell.2015.09.057

- Ma, S., Rong, Z., Liu, C., Qin, X., Zhang, X. and Chen, Q. (2021). DNA damage promotes microtubule dynamics through a DNA-PK-AKT axis for enhanced repair. *J. Cell Biol.* **220**, e201911025. doi:10.1083/jcb.201911025
- Mcvey, M., Lee, S. E., Avenue, H. and Antonio, S. (2008). MMEJ repair of double-strand breaks (director's cut): deleted sequences and alternative endings. *Trends Genet.* **24**, 529-538. doi:10.1016/j.tig.2008.08.007
- Mehta, A. and Haber, J. E. (2014). Sources of DNA double-strand breaks and models of recombinational DNA Repair. *Cold Spring Harb. Perspect. Biol.* **6**, a016428. doi:10.1101/cshperspect.a016428
- Menin, L., Colombo, C. V., Maestrini, G., Longhese, M. P. and Clerici, M. (2019). TEL1/ATM signaling to the checkpoint contributes to replicative senescence in the absence of telomerase. *Genetics* **213**, 411-429. doi:10.1534/genetics.119.302391
- Miné-Hattab, J. and Rothstein, R. (2012). Increased chromosome mobility facilitates homology search during recombination. *Nat. Cell Biol.* **14**, 510-517. doi:10.1038/ncb2472
- Miné-Hattab, J., Recamier, V., Izeddin, I., Rothstein, R. and Darzacq, X. (2017). Multi-scale tracking reveals scale-dependent chromatin dynamics after DNA damage. *Mol. Biol. Cell* **28**, 3323-3332. doi:10.1091/mbc.e17-05-0317
- Mirman, Z. and de Lange, T. (2020). 53BP1: a DSB escort. *Genes Dev.* **34**, 7-23. doi:10.1101/gad.333237.119
- Moore, J. D., Yazgan, O., Ataian, Y. and Krebs, J. E. (2007). Diverse roles for histone H2A modifications in DNA damage response pathways in yeast. *Genetics* **176**, 15-25. doi:10.1534/genetics.106.063792
- Morrison, A. J., Highland, J., Krogan, N. J., Arbel-Eden, A., Greenblatt, J. F., Haber, J. E. and Shen, X. (2004). INO80 and γ -H2AX interaction links ATP-dependent chromatin remodeling to DNA damage repair. *Cell* **119**, 767-775. doi:10.1016/j.cell.2004.11.037
- Nakada, D., Matsumoto, K. and Sugimoto, K. (2003). ATM-related Tel1 associates with double-strand breaks through an Xrs2-dependent mechanism. *Genes Dev.* **17**, 1957-1962. doi:10.1101/gad.1099003
- Pelliccioli, A., Lee, S. E., Lucca, C., Foiani, M. and Haber, J. E. (2001). Regulation of Saccharomyces Rad53 checkpoint kinase during adaptation from DNA damage-induced G2/M arrest. *Mol. Cell* **7**, 293-300. doi:10.1016/S1097-2765(01)00177-0
- Qian, M.-X., Pang, Y., Liu, C. H., Haratake, K. and Du, B.-Y., Ji, D.-Y., Wang, G.-F., Zhu, Q.-Q., Song, W., Yu, Y. et al. (2013). Acetylation-mediated proteasomal degradation of core histones during DNA repair and spermatogenesis. *Cell* **153**, 1012-1024. doi:10.1016/j.cell.2013.04.032
- Redon, C., Pilch, D. R., Rogakou, E. P., Orr, A. H., Lowndes, N. F. and Bonner, W. M. (2003). Yeast histone 2A serine 129 is essential for the efficient repair of checkpoint-blind DNA damage. *EMBO Rep.* **4**, 678-684. doi:10.1038/sj.embo.embor.871
- Reina-San-Martin, B., Difilippantonio, S., Hanitsch, L., Masilamani, R. F., Nussenzweig, A. and Nussenzweig, M. C. (2003). H2AX is required for recombination between immunoglobulin switch regions but not for intra-switch region recombination or somatic hypermutation. *J. Exp. Med.* **197**, 1767-1778. doi:10.1084/jem.20030569
- Renkawitz, J., Lademann, C. A., Kalocsay, M. and Jentsch, S. (2013). Monitoring homology search during DNA double-strand break repair in vivo. *Mol. Cell* **50**, 261-272. doi:10.1016/j.molcel.2013.02.020
- Robinett, C. C., Straight, A., Li, G., Wilhelm, C., Sudlow, G., Murray, A. and Belmont, A. S. (1996). In vivo localization of DNA sequences and visualization of large-scale chromatin organization using lac operator/repressor recognition. *J. Cell Biol.* **135**, 1685-1700. doi:10.1083/jcb.135.6.1685
- Rossetto, D., Avvakumov, N. and Côté, J. (2012). Histone phosphorylation: a chromatin modification involved in diverse nuclear events. *Epigenetics* **7**, 1098-1108. doi:10.4161/epi.21975
- Ryu, T., Spatola, B., Delabaere, L., Bowlin, K., Hopp, H., Kunitake, R., Karpen, G. H. and Chiolo, I. (2015). Heterochromatic breaks move to the nuclear periphery to continue recombinational repair. *Nat. Cell Biol.* **17**, 1401-1411. doi:10.1038/ncb3258
- Schrank, B. R., Aparicio, T., Li, Y., Chang, W., Chait, B. T., Gundersen, G. G., Gottesman, M. E. and Gautier, J. (2018). Nuclear ARP2/3 drives DNA break clustering for homology-directed repair. *Nature* **559**, 61-66. doi:10.1038/s41586-018-0237-5
- Seeber, A., Dion, V. and Gasser, S. M. (2013). Checkpoint kinases and the INO80 nucleosome remodeling complex enhance global chromatin mobility in response to DNA damage. *Genes Dev.* **27**, 1999-2008. doi:10.1101/gad.222992.113
- Seeber, A., Hauer, M. H. and Gasser, S. M. (2018). Chromosome dynamics in response to DNA damage. *Annu. Rev. Genet.* **52**, 295-319. doi:10.1146/annurev-genet-120417-031334
- Sellou, H., Lebeauin, T., Chapuis, C., Smith, R., Hegele, A., Singh, H. R., Kozlowski, M., Bultmann, S., Ladurner, A. G., Timinszky, G. et al. (2016). The poly(ADP-ribose)-dependent chromatin remodeler Alc1 induces local chromatin relaxation upon DNA damage. *Mol. Biol. Cell* **27**, 3791-3799. doi:10.1091/mbc.16-05-0269
- Shaltiel, I. A., Krenning, L., Bruinsma, W. and Medema, R. H. (2015). The same, only different - DNA damage checkpoints and their reversal throughout the cell cycle. *J. Cell Sci.* **128**, 607-620. doi:10.1242/jcs.163766
- Shroff, R., Arbel-Eden, A., Pilch, D., Ira, G., Bonner, W. M., Petrini, J. H., Haber, J. E. and Lichten, M. (2004). Distribution and dynamics of chromatin modification induced by a defined DNA double-strand break. *Curr. Biol.* **14**, 1703-1711. doi:10.1016/j.cub.2004.09.047
- Smith, M. J. and Rothstein, R. (2017). Poetry in motion: increased chromosomal mobility after DNA damage. *DNA Repair*, **56**, 102-108. doi:10.1016/j.dnarep.2017.06.012
- Smith, M. J., Bryant, E. E. and Rothstein, R. (2018). Increased chromosomal mobility after DNA damage is controlled by interactions between the recombination machinery and the checkpoint. *Genes Dev.* **32**, 1242-1251. doi:10.1101/gad.317966.118
- Smith, R., Lebeauin, T., Juhász, S., Chapuis, C., D'Augustin, O., Dutertre, S., Burkovics, P., Biertümpfel, C., Timinszky, G. and Huet, S. (2019). Poly(ADP-ribose)-dependent chromatin unfolding facilitates the association of DNA-binding proteins with DNA at sites of damage. *Nucleic Acids Res.* **47**, 11250-11267. doi:10.1093/nar/gkz820
- Soutoglou, E. and Misteli, T. (2008). Activation of the cellular DNA damage response in the absence of DNA lesions. *Science* **320**, 1507-1510. doi:10.1126/science.1159051
- Spichal, M., Brion, A., Herbert, S., Cournac, A., Marbouty, M., Zimmer, C., Koszul, R. and Fabre, E. (2016). Evidence for a dual role of actin in regulating chromosome organization and dynamics in yeast. *J. Cell Sci.* **129**, 681-692. doi:10.1242/jcs.175745
- Strecker, J., Gupta, G. D., Zhang, W., Bashkurov, M., Landry, M.-C., Pelletier, L. and Durocher, D. (2016). DNA damage signalling targets the kinetochore to promote chromatin mobility. *Nat. Cell Biol.* **18**, 281-290. doi:10.1038/ncb3308
- Sweeney, F. D., Yang, F., Chi, A., Shabanowitz, J., Hunt, D. F. and Durocher, D. (2005). Saccharomyces cerevisiae Rad9 acts as a Mec1 adaptor to allow Rad53 activation. *Curr. Biol.* **15**, 1364-1375. doi:10.1016/j.cub.2005.06.063
- Symington, L. S. and Gautier, J. (2011). Double-strand break end resection and repair pathway choice. *Annu. Rev. Genet.* **45**, 247-271. doi:10.1146/annurev-genet-110410-132435
- Tibbetts, R. S., Brumbaugh, K. M., Williams, J. M., Sarkaria, J. N., Cliby, W. A., Shieh, S.-Y., Taya, Y., Prives, C. and Abraham, R. T. (1999). A role for ATR in the DNA damage-induced phosphorylation of p53. *Genes Dev.* **13**, 152-157. doi:10.1101/gad.13.2.152
- Tsukuda, T., Fleming, A. B., Nickoloff, J. A., Osley, M. A. (2005). Chromatin remodelling at a DNA double-strand break site in saccharomyces cerevisiae. *Nature* **438**, 379-383. doi:10.1038/nature04148
- Van Attikum, H., Fritsch, O. and Gasser, S. M. (2004). Recruitment of the INO80 complex by H2A phosphorylation links ATP-dependent chromatin remodeling with DNA double-strand break repair. *Cell* **119**, 777-788. doi:10.1016/j.cell.2004.11.033
- van Attikum, H., Fritsch, O. and Gasser, S. M. (2007). Distinct roles for SWR1 and INO80 chromatin remodeling complexes at chromosomal double-strand breaks. *EMBO J.* **26**, 4113-4125. doi:10.1038/sj.emboj.7601835
- Waterman, D. P., Zhou, F., Li, K., Lee, C.-S., Tsabar, M., Eapen, V. V., Mazzella, A. and Haber, J. E. (2019). Live cell monitoring of double strand breaks in S. Cerevisiae. *PLoS Genet.* **15**, e1008001. doi:10.1371/journal.pgen.1008001
- Weinert, T. A. and Hartwell, L. H. (1988). The RAD9 gene controls the cell cycle response to DNA damage in Saccharomyces cerevisiae. *Science* **241**, 317-322. doi:10.1126/science.3291120
- Zhou, B.-B. S. and Elledge, S. J. (2000). The DNA damage response: putting checkpoints in perspective. *Nature* **408**, 433-439. doi:10.1038/35044005
- Zimmer, C. and Fabre, E. (2019). Chromatin mobility upon DNA damage: state of the art and remaining questions. *Curr. Genet.* **65**, 1-9. doi:10.1007/s00294-018-0852-6
- Zimmermann, M. and De Lange, T. (2014). 53BP1: pro choice in DNA repair. *Trends Cell Biol.* **24**, 108-117. doi:10.1016/j.tcb.2013.09.003
- Ziv, Y., Bielopolski, D., Galanty, Y., Lukas, C., Taya, Y., Schultz, D. C., Lukas, J., Bekker-Jensen, S., Bartek, J. and Shiloh, Y. (2006). Chromatin relaxation in response to DNA double-strand breaks is modulated by a novel ATM-and KAP-1 dependent pathway. *Nat. Cell Biol.* **8**, 870-876. doi:10.1038/ncb1446



Supplementary Figure 1

Figure S1.

Absence of growth defects and intrinsic DNA damages in H2A-S129E mutant.

A. Representative growth curves for the WT, H2A-S129A, H2AS129E strains in the absence (left) or presence (right) of 250µg/ml Zeocin treatment. Mean values for two independent experiments are plotted for each time point, with error bars showing standard error of the mean (SE).

B. No intrinsic DNA damage in H2A-S129E in absence of Zeocin treatment but prolonged exposure to Zeocin increases DNA damage. Rad52-GFP foci are shown (arrowheads) in representative images of yeast cells that were either untreated or exposed to 250µg/ml of the genotoxic drug Zeocin for 4 and 6 h in WT (black) and H2A-S129E strain (grey). Bar graphs show mean \pm s.e.m. P values are calculated after a non-parametric t test (n.s, not significant $P>0.05$).

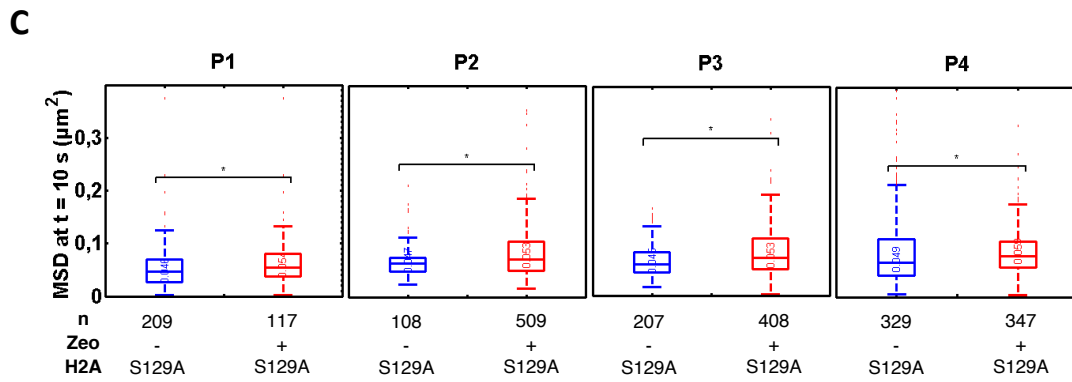
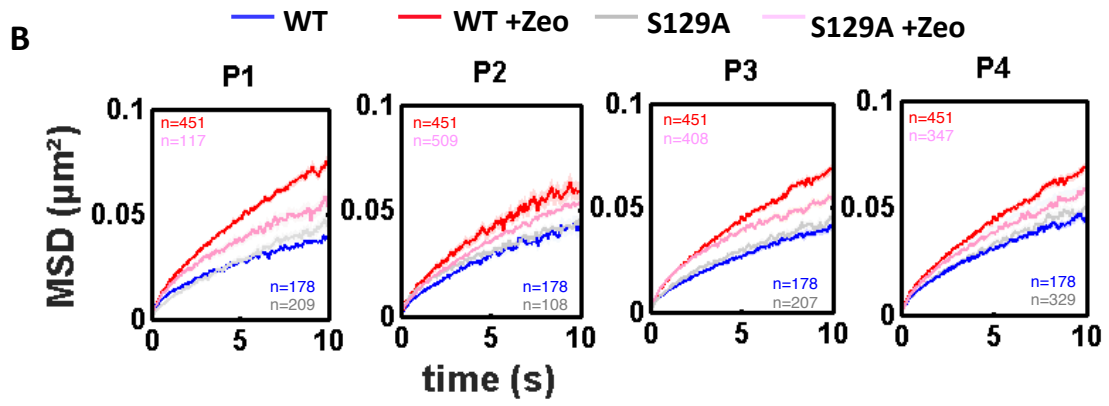
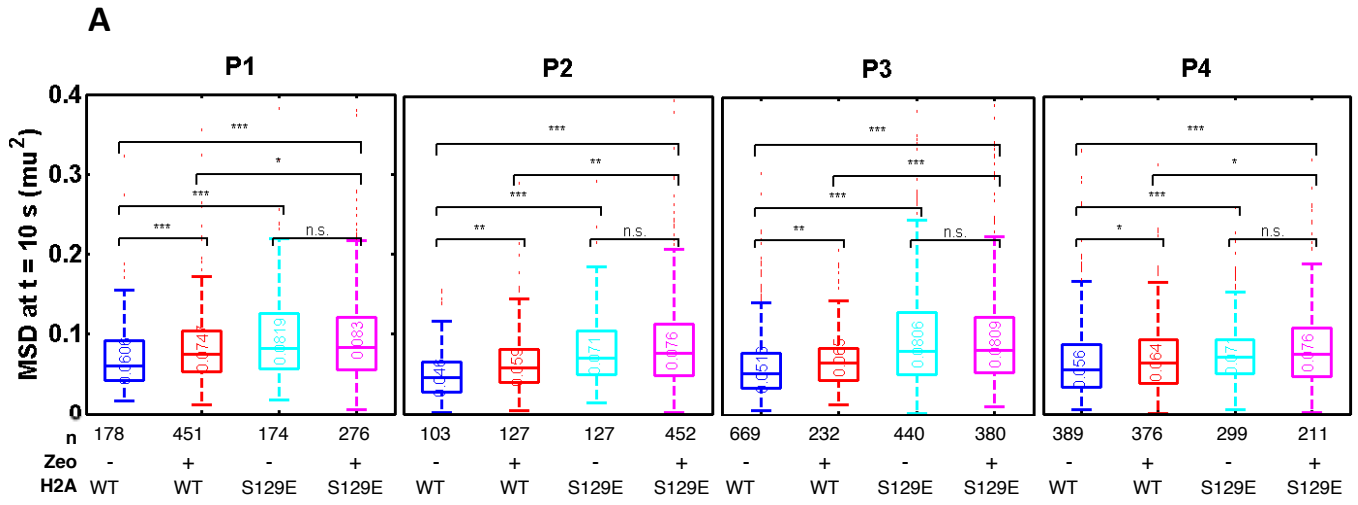


Figure S2.

Values of MSDs at 10 sec. in WT, H2A-S129E and H2A-S19E mutated strains

A. Values of MSD at 10 sec for WT, H2A-S129E and H2A-S129A. Boxplots show the distribution of MSD at 10 s in absence of Zeocin (WT, blue; H2A-S129E, light blue) or after 3 h Zeocin exposure (WT, red; H2A-S129E, pink), for the four loci Gr1–Gr4. The horizontal line at the center of each box indicates the median value, the bottom and top limits indicate the lower and upper quartiles, respectively. The whiskers indicate the full range of measured values, except for outliers, which are shown as small red dots. Brackets indicate the result of a Wilcoxon rank-sum test between distributions, with “n.s.” for “not significant” ($P > 0.05$), * for $P < 0.05$, ** for $P < 10^{-2}$ and *** for $P < 10^{-3}$.

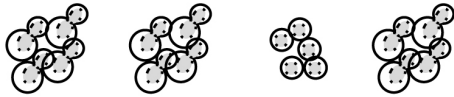
B. MSDs for WT and H2A-S129A. Mean square displacement measured as in figure 1D as function of time interval of the four Gr1 to Gr4 green loci in H2A-S129A background. Blue and red curves are for untreated and treated Wild-Type cells (WT); grey and pink curves are for untreated and treated H2A-S129A mutant, respectively. The numbers of cells used to compute each curve (n) are indicated.

C. Values of MSD at 10 sec for H2A-S129A in the presence or absence of treatment. Boxplots show the distribution of MSD at 10 s as in B, in absence of Zeocin (blue) or after 3 h Zeocin exposure (red), for the four loci Gr1–Gr4 in H2A-S129A mutated background.

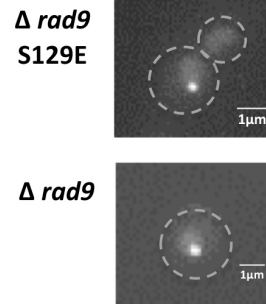
A

% of G2/M arrested cells

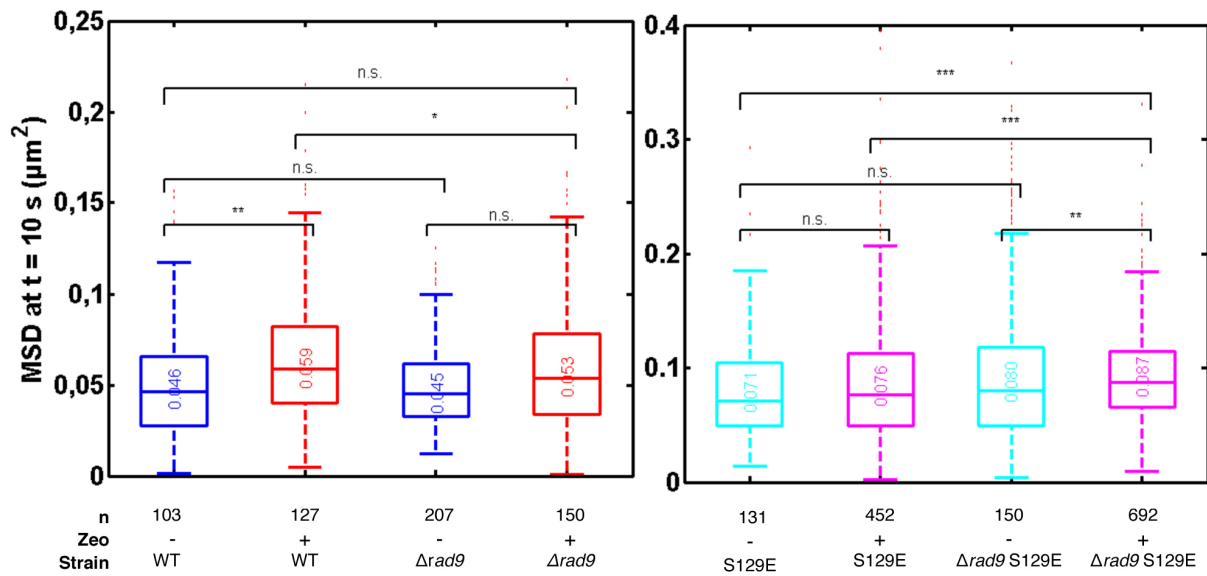
	WT		H2A-S129E		$\Delta rad9$		$\Delta rad9$ H2A-S129E	
ZEO	-	+	-	+	-	+	-	+
%	10	92	9	89	3	4	7	94



+ Zeo



B



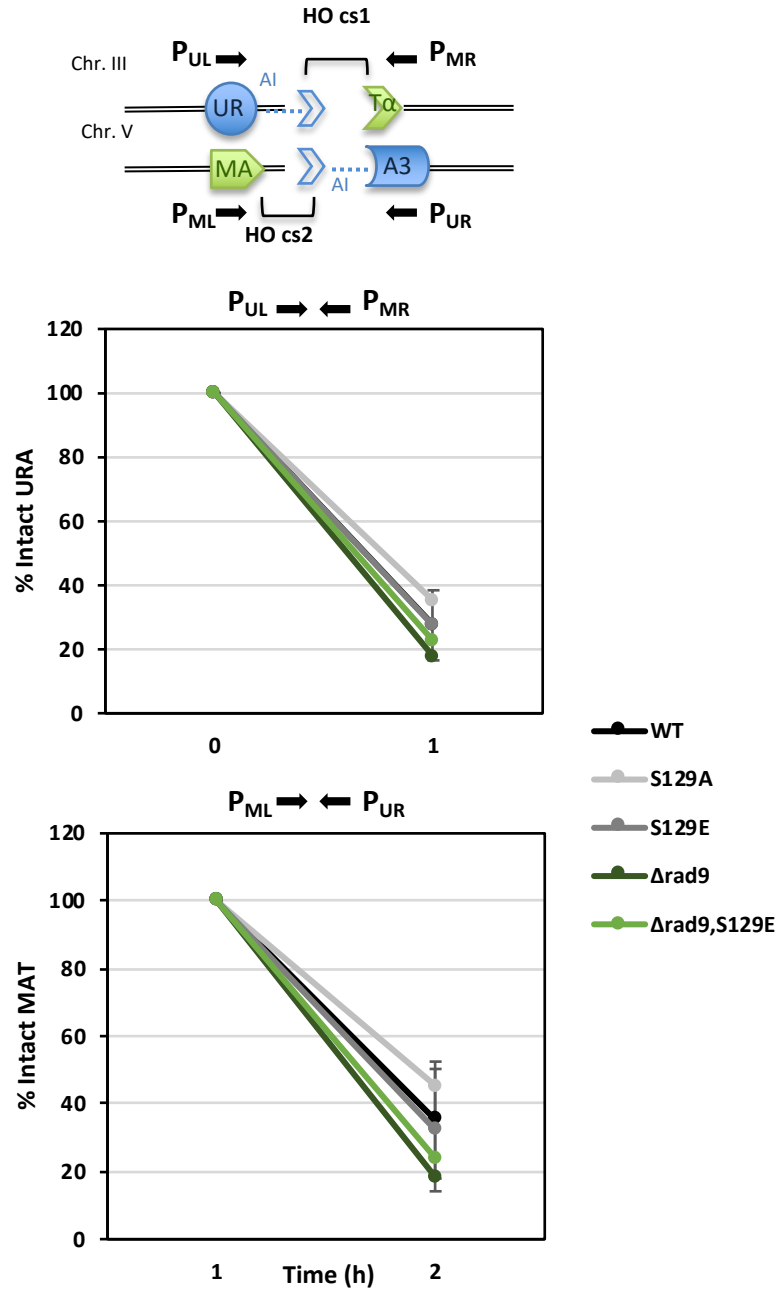
Supplementary Figure 3

Figure S3.

Percent of G2/M arrested cells and values of MSD at 10 sec for WT, H2A-S129E, $\Delta rad9$ and $\Delta rad9$ H2A-S129E mutated cells in the absence or the presence of Zeocin for.

A. Cells expressing fluorescent LacI-GFP protein to lacO-array were inspected after image acquisition. Unbound LacI-GFP was used as a nuclear staining. G2/M arrested cells show nuclear masses separated between mother and daughter cells, but no septum formed. Examples are shown on the right.

B. Boxplots show the distribution of MSD at 10 s of WT compared to $\Delta rad9$ strains (left) and H2A-S129E compared to $\Delta rad9$ H2A-S129E double mutant (right) in absence of Zeocin (bleu and cyan, respectively) or after 6 h Zeocin exposure (red and magenta, respectively). The horizontal line at the center of each box indicates the median value, the bottom and top limits indicate the lower and upper quartiles, respectively. The whiskers indicate the full range of measured values, except for outliers, which are shown as small red dots. Brackets indicate the result of a Wilcoxon rank-sum test between distributions, with “n.s.” for “not significant” ($P > 0.05$), * for $P < 0.05$, ** for $P < 10^{-2}$ and *** for $P < 10^{-3}$. Analyzed cells range from (n) ~100 - ~1000.



Supplementary Figure 4

Figure S4

Efficiency of the two HO-cleavages in translocation assay strains by Q-PCR.

Efficiency of HO cleavage in WT, H2A-S129A, H2A-S129E, $\Delta rad9$ and $\Delta rad9$, H2A-S129E strains carrying the two HO cleavage sites at the $MAT\alpha$ and $URA3$ locus was determined by quantitative PCR using primers flanking HO recognition sites before (t0h) and after (t1h) galactose induction, normalized by the amount of $ACT1$ sequence.

STRAINS			
Common name	Strain	Genotype	Reference
Green-Red pairs			
P1	YHB76-4-a	Mat a, ura3Δ0, leu2Δ0, his3Δ1, lys2Δ202, ade2-661, can1::HPHMX, iYGL117::tetR-mRFP- NATMX, yDR003W::tetO-TEF-URA, HIS3::HIS3-LacI-GFP, yDR095C::256lacO-TEF-LEU2	(Herbert:2017it)
P2	YHB103-1-a	Mat a, ura3Δ0, leu2Δ0, his3Δ1, lys2Δ202, ade2-661, can1::HPHMX, iYGL117::tetR-mRFP- NATMX, yDR199W::tetO-TEF-URA3, HIS3::HIS3-LacI-GFP, yDR297W::256lacO-TEF-LEU2	(Herbert:2017it)
P3	YHB215-2-alpha	Mat alpha, ura3Δ0, leu2Δ0, his3Δ1, lys2Δ202, ade2-661, iYGL117::tetR-mRFP- NATMX, yDR354W::tetO-TEF-URA3, HIS3::HIS3-LacI-GFP, yDR259C::256lacO-TEF-LEU2	(Herbert:2017it)
P4	YHB154-1-alpha	Mat alpha, ura3Δ0, leu2Δ0, his3Δ1, ade2-661, yDR539W::112tetO-TEF-URA3, iYGL117::tetR-mRFP- NATMX, HIS3::HIS3-LacI-GFP, yDR445C::256lacO-TEF-LEU2	(Herbert:2017it)
H2A mutants			
P1 S129E	YEF 1259	Mat a, ura3Δ0, leu2Δ0, his3Δ1, lys2Δ202, ade2-661, can1::HPHMX, iYGL117::tetR-mRFP NATMX yDR003W::tetO-URA3 HIS3::HIS3-LacI-GFP yDR095C::lacO-TEF-LEU2, hta1::HTA1-S129E, hta2::HTA2-S129E	This study
P2 S129E	YEF 1111	Mat a, ura3Δ0, leu2Δ0, his3Δ1, lys2Δ202, ade2-661, can1::HPHMX, iYGL117::tetR-mRFP NATMX yDR199W::tetO-URA3 HIS3::HIS3-LacI-GFP yDR297W::lacO-TEF-LEU2, hta1::HTA1-S129E, hta2::HTA2-S129E	This study
P3 S129E	YEF 1261	Mat a, ura3Δ0, leu2Δ0, his3Δ1, lys2Δ202, ade2-661, iYGL117::tetR-mRFP NATMX yDR354W::tetO-URA3 HIS3::HIS3-LacI-GFP yDR259C::lacO-TEF-LEU2, hta1::HTA1-S129E, hta2::HTA2-S129E	This study
P4 S129E	YEF 1163	Mat alpha, ura3Δ0, leu2Δ0, his3Δ1, ade2-661, yDR539W::112tetO-TEF-URA3, iYGL117::tetR-mRFP NATMX yDR354W::tetO-URA3 HIS3::HIS3-LacI-GFP yDR445C::lacO-TEF-LEU2, hta1::HTA1-S129E, hta2::HTA2-S129E	This study
P1 S129A	YEF 1030	Mat a, ura3Δ0, leu2Δ0, his3Δ1, lys2Δ202, ade2-661, can1::HPHMX, iYGL117::tetR-mRFP NATMX yDR003W::tetO-URA3 HIS3::HIS3-LacI-GFP yDR095C::lacO-TEF-LEU2, hta1::HTA1-S129A-KANMX, hta2::HTA2-S129A-ADE2	(Herbert:2017it)
P2 S129A	YEF 1028	Mat a, ura3Δ0, leu2Δ0, his3Δ1, lys2Δ202, ade2-661, can1::HPHMX, iYGL117::tetR-mRFP NATMX yDR199W::tetO-URA3 HIS3::HIS3-LacI-GFP yDR297W::lacO-TEF-LEU2, hta1::HTA1-S129A-KANMX, hta2::HTA2-S129A-ADE2	(Herbert:2017it)
P3 S129A	YEF 1032	Mat a, ura3Δ0, leu2Δ0, his3Δ1, lys2Δ202, ade2-661, iYGL117::tetR-mRFP NATMX yDR354W::tetO-URA3 HIS3::HIS3-LacI-GFP yDR259C::lacO-TEF-LEU2, hta1::HTA1-S129A-KANMX, hta2::HTA2-S129A-ADE2	(Herbert:2017it)
P4 S129A	YEF 1034	Mat alpha, ura3Δ0, leu2Δ0, his3Δ1, ade2-661, yDR539W::112tetO-TEF-URA3, iYGL117::tetR-mRFP NATMX yDR354W::tetO-URA3 HIS3::HIS3-LacI-GFP yDR445C::lacO-TEF-LEU2, hta1::HTA1-S129A-KANMX, hta2::HTA2-S129A-ADE2	(Herbert:2017it)
rad9 mutants			
P2 rad9	YEF 1187	Mat a, ura3Δ0, leu2Δ0, his3Δ1, lys2Δ202, ade2-661, can1::HPHMX, iYGL117::tetR-mRFP NATMX yDR199W::tetO-URA3 HIS3::HIS3-LacI-GFP yDR297W::lacO-TEF-LEU2, yDR217C::KANMX	This study
P2 rad9 S129E	YEF 1188	Mat a, ura3Δ0, leu2Δ0, his3Δ1, lys2Δ202, ade2-661, can1::HPHMX, iYGL117::tetR-mRFP NATMX yDR199W::tetO-URA3 HIS3::HIS3-LacI-GFP yDR297W::lacO-TEF-LEU2, hta1::HTA1-S129E, hta2::HTA2-S129E, yDR217C::KANMX	This study
Repair Assay			
Δku70	YEF571	Mat a, ura3Δ0, leu2Δ0, his3Δ1, trp1Δ63, ade2-661, yMR284W::KANMX	Euroscarf
Translocation Assay			
Tr WT	YEF 1375	ho Δ MATA3 ⁺ ::intron:ura3Δ5 ⁺ hmlΔ::ADE1 hmrΔ::ADE1 ura3Δ3 ⁺ ::intron::Hocs ade3 ⁺ ::GAL::HO	(Lee:2008it)
Tr S129E	YEF 1377	ho Δ MATA3 ⁺ ::intron:ura3Δ5 ⁺ hmlΔ::ADE1 hmrΔ::ADE1 ura3Δ3 ⁺ ::intron::Hocs ade3 ⁺ ::GAL::HO, hta1::HTA1-S129E, hta2::HTA2-S129E	This study
Tr S129A	YEF 1378	ho Δ MATA3 ⁺ ::intron:ura3Δ5 ⁺ hmlΔ::ADE1 hmrΔ::ADE1 ura3Δ3 ⁺ ::intron::Hocs ade3 ⁺ ::GAL::HO, hta1::HTA1-S129A, hta2::HTA2-S129A	This study
Tr rad9	YEF 1405	ho Δ MATA3 ⁺ ::intron:ura3Δ5 ⁺ hmlΔ::ADE1 hmrΔ::ADE1 ura3Δ3 ⁺ ::intron::Hocs ade3 ⁺ ::GAL::HO, yDR217C::KANMX	This study
Tr rad9 S129E	YEF 1406	ho Δ MATA3 ⁺ ::intron:ura3Δ5 ⁺ hmlΔ::ADE1 hmrΔ::ADE1 ura3Δ3 ⁺ ::intron::Hocs ade3 ⁺ ::GAL::HO, hta1::HTA1-S129E, hta2::HTA2-S129E, yDR217C::KANMX	This study
SPB-Cen4 strains			
WT	YEF 1019	CENIV-tetO, tetR-GFP, spc42::SPC42::mCherry-HIS3	This study
H2A S129E	YEF 1364	CENIV-tetO, tetR-GFP, spc42::SPC42::mCherry-HIS3, hta1::HTA1-S129E, hta2::HTA2-S129E	This study
H2A S129A	YEF 1366	CENIV-tetO, tetR-GFP, spc42::SPC42::mCherry-HIS3, hta1::HTA1-S129A, hta2::HTA2-S129A	This study
PLASMIDS			
Name	Description	Marker	Reference
pEF562	ycas9- PHU91	KANMX (ARS-CEN)	J. Haber
pEF567	pEF562+guide HTA1	KANMX (ARS-CEN)	This study
pEF568	pEF562+guide HTA2	KANMX (ARS-CEN)	This study
PRS413	PRS413 (SacI site)	HIS3 (ARS-CEN)	Addgene
PRIMERS			
Name	Description	Sequence	Reference
pFGF 001	HTA1 guide forward	CTTCTCAAGAATTATAAGATGTTTT	This study
pFGF 002	HTA1 guide reverse	ATCTTATAAATCTTGAGAAGGATCA	This study
pFGF 003	HTA2 guide forward	TTACAGTCTCTTGAGAAGCTTTGTTTT	This study
pFGF 004	HTA2 guide reverse	AAGCTTCTCAAGAACTGTAGATCA	This study
pFGF 005	AmpB reverse	AGCTGAATGAAGCCATCAACCAACGA	This study
pFGF 006	80 nt donor sequence for HTA1	GAAGTCTGCCAAGGCTCAAGGCTGAACAAGAATTATAAGATCGGTCTGGTATTTAAAGAAAGCGGAA	This study
pFGF 007	80 nt donor sequence for HTA2	CAAACTTGTGCCAAGAAGCTGCCAAGACTGCCAAGCTGaaCAAGAAGCTGTAAGAAGCTGAGTTAAAAGAAACAAA	This study
pFGF 008	HTA1 verification forward	GTTGCCAAGAAGCTGCCTCA	This study
pFGF 009	HTA1 verification reverse	TGGAGAAGCAGTTTGTATTCCTT	This study
pFGF 010	HTA2 verification forward	AATGTTACCATCGCCCAAGG	This study
pFGF 011	HTA2 verification reverse	ACCAGTCTTCTCATATGACCT	This study
pFGF 012	rad9 integration forward	ACGGCCTTGTGAGCGTTAGA	This study
pFGF 013	rad9 integration reverse	CCATTGGGGTGAAGCTTCGTT	This study
pFGF 014	rad9 verification forward	TCAAGGGGAAGGTGTCAGCAA	This study
pFGF 015	rad9 verification reverse	TGCTGATATGTGTCTGCCA	This study
pFGF 016	m13 forward	GTAAACGACGGCCAGT	Addgene
pFGF 017	m13 inverse	GTCATAGCTGTTCTCG	Addgene

Table S1. Strains, plasmids and primers used in this study.